Insights from scanning tunneling microscopy experiments into correlated electron systems

Benschop, T.

Appendix A

Supplementary information to puddle formation, persistent gaps, and non-mean-field breakdown of superconductivity in overdoped $(Pb,Bi)_2Sr_2CuO_{6+\delta}$

Significant contributions to this appendix have been made by Willem O. Tromp and Miguel A. Sulangi.

A.1 Experimental Methods

We performed a systematic study on a series of $(Pb,Bi)_2Sr_2CuO_{6+\delta}$ samples with 8 distinct doping levels, covering the range from underdoped (UD25K) to strongly overdoped (OD0K) side. Single crystal samples were grown by the conventional floating-zone technique [39,53]. The UD25K, OP35K, and OD15K samples contain La doping, i.e. $(Pb,Bi)_2(La,Sr)_2CuO_{6+\delta}$, while the rest of the samples are without La doping. The doping levels, transition temperatures Tc, and measurement temperatures are listed in table A.1. The doping levels of the superconducting samples are determined using the Presland formula, while the doping level of the OD0K sample is extracted from the rigid band shift measured by ARPES (see supplementary section A.5). All samples were cleaved *in situ* in a cryogenic environment and inserted immediately into the STM. The data were acquired using different home-built cryogenic STMs among three groups.

Name	Doping	Tc (K)	Measurement T (K)	Data acquired by
UD25K	0.101	25	5.7	Hudson group
OP35K	0.160	35	5.7	Hudson group
OD23K	0.224	23	4.2	Allan group
OD15K	0.243	15	6	Hoffman group
OD12K	0.249	12	4.2	Allan group
OD9K	0.255	9	4.2 - 20	Allan group
OD7K	0.258	7	2.2	Allan group
OD3K	0.265	3	4.2	Allan group
OD0K	0.274		4.2	Allan group

Table A.1: Samples and their measurement conditions in this study.

A.2 The phenomenological model to fit spectra

A.2.1 The d-wave gap model

The d-wave gap is here modeled as a mean of multiple s-wave gaps, one for each point along the Fermi Surface. For each s-wave gap, the gap size Δ_k is given by $\Delta_k = \Delta\left(\cos(k_x) - \cos(k_y)\right)/2$. The points k_x, k_y are found using the Fermi Surface of the tight-binding model for the OD15K sample1 although the final shape of the spectrum varies a lot with the exact points in k-space used. Each s-wave gap is generated by using the Dynes formula:

$$\text{Dynes}\left(E, \Delta_k, \Gamma\right) = \text{Re}\left(\frac{E + i\Gamma}{\sqrt{(E + i\Gamma)^2 - {\Delta_k}^2}}\right), \tag{A.1}$$

Name	Samples fabricated by	V_{setup} (mV) / I_{setup} (pA) / Lock-In amplitude (mV)	Effective energy resolution (FWHM, mV)
UD25K	Kondo group	-100/400/1	2.7
OP35K	Kondo group	-100/400/1	2.7
OD23K	UvA group	-150/150/1.5	2.58
OD15K	Kondo group	-100/100/2	3.5
OD12K	UvA group	200/170/1.5	2.58
OD9K	UvA group	150/200/1.5	2.58 - 6.42
OD7K	UvA group	-20/600/1.5	2.50
OD3K	UvA group	200/170/1.5	2.58
OD0K	UvA group	-25/200/1.5	2.58

Table A.2: Samples and their measurement conditions in this study.

where the same Γ is used for all s-wave gaps. The resulting d-wave gap is the mean of all s-wave gaps. To account for the normal-state density of states (DOS), the d-wave gap function is multiplied with a polynomial function, typically of the 3rd order. The resulting spectrum is then convoluted with a Gaussian function with a full width at half maximum (FWHM) given in the table above, in order to emulate the effect of finite temperature and the lock-in modulation have on the shape of the measured spectrum.
The points in momentum space are calculated only once before the fitting process to reduce computation time. The fitting parameters characterizing the gap are only Δ and Γ. To calculate the filling for the d-wave gap we calculate the mean of the filling for each individual s-wave gap using $F = [1 + (\Delta/\Gamma)^2]^{-\frac{1}{2}}$.

A.2.2 Statistical analysis with and without the excluded spectra

In the main text we "white out" certain spectra (white areas in figure 2.3b-d), and exclude them for the statistical analysis when either of the two conditions is met in the fit results: 1) $\Gamma > 20$ meV; 2) $\Delta > 15$ meV. Our interpretation is that these spectra are fully filled, for the following reason: the spectra that meet the first criterion have so much broadening that there is no well-defined gap. Similarly, for the spectra that meet the second criterion, the large "gap" is a reflection of background modulations. Such spectra are thus counted as fully filled. Still, we show here that including these spectra in the analysis does not alter our main conclusions.

Figure A.1 shows, from left to right, the spatial distributions of: Δ, including "whited-out" (1st column) and excluding "whited-out" (2nd column) spectra, Γ, with (3rd column) and without (4th column) "whited-out" spectra, and F, the filling (5th column)

for all samples. The images are ordered top to bottom, from lowest to highest doping, respectively. Following the argumentation in the preceding paragraph, the filling for "whited-out" spectra is set to 1, when they are included in the statistics. Figure A.2 shows the histograms for Δ including "whited-out" spectra, and the histograms of Γ, both with and without "whited-out" spectra. The remaining histograms of Δ excluding the "whited-out" spectra and of the filling can be found in the main text. The histograms in figure A.2 are summarized in figure A.3 in a similar fashion to figure 2.4 of the main text. From the spatial distributions and histograms of Δ and Γ in figure A.1-A.3, we conclude that even when the "whited-out" spectra are considered: 1) the gap size still deviates from the $\Delta \sim$Tc behavior in the OD regime; 2) gapped spectra can still be found in the non-SC sample in significant quantities. The spatial averages of the "whited-out" spectra and of the rest spectra are shown in figure A.4 for each sample. We find that after whiting out all samples, even the non-SC sample, show a gap in their average spectrum. We note that the spatially-averaged "whited-out" spectra in the OD regime are fully filled, i.e. they no longer have a gap, and often show a peak near Fermi level. This further justifies our choice to assign all these spectra a filling of 1. For the UD25K and OPT35K samples, the "whited-out" spectra are made up of spectra for which the fit has failed due to limited signal-to-noise. Even though these spectra appear as gapped, we attribute this to the presence of a pseudogap. We find that the assignment of $F = 1$ to these spectra does not alter the main conclusion either, given the relatively small portions of "whited-out" spectra in these samples (see figure A.4). The increase of the area of "whited out spectra" in the OD as shown in figure A.4 reaffirms the increased gap filling in these samples.

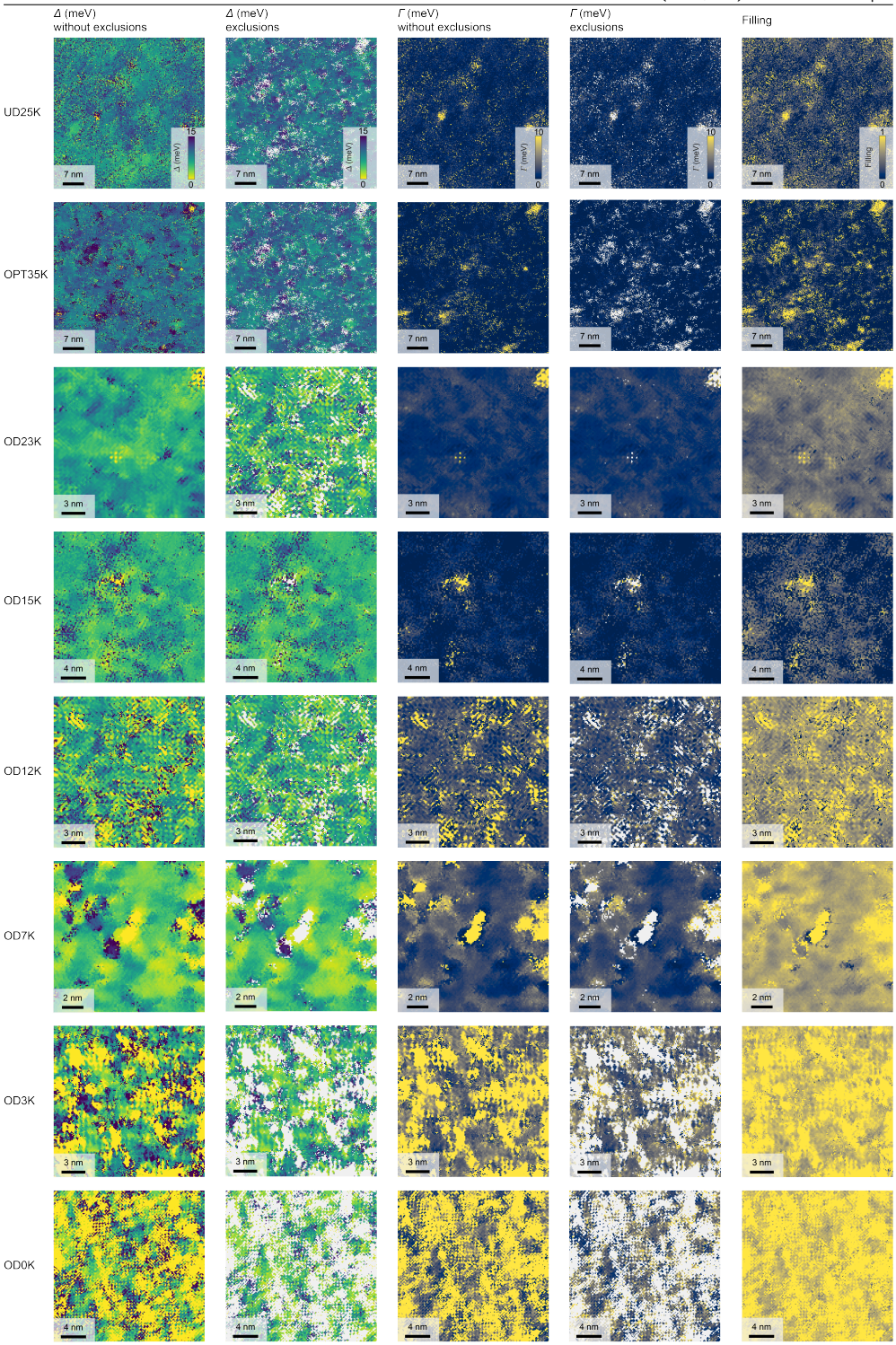

Figure A.1: Spatial variations of the gap size Δ with and without exclusions, parameter Γ with and without exclusions, and the calculated filling for all samples. See text for details.

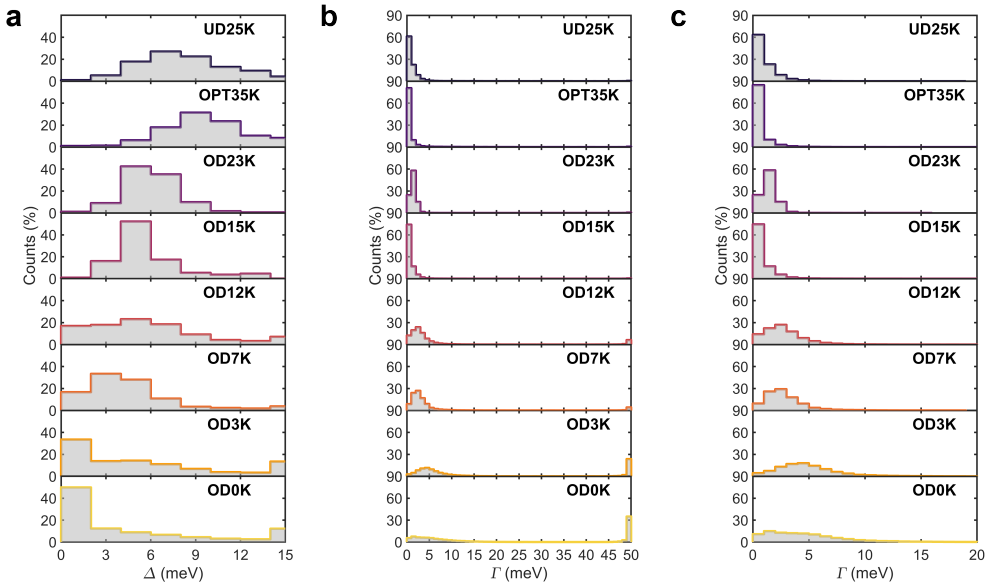

Figure A.2: a) Histograms of the gap size Δ without any spectra that are whited out. Histograms for Γ including (b) and excluding (c) whited-out spectra. See text for details.

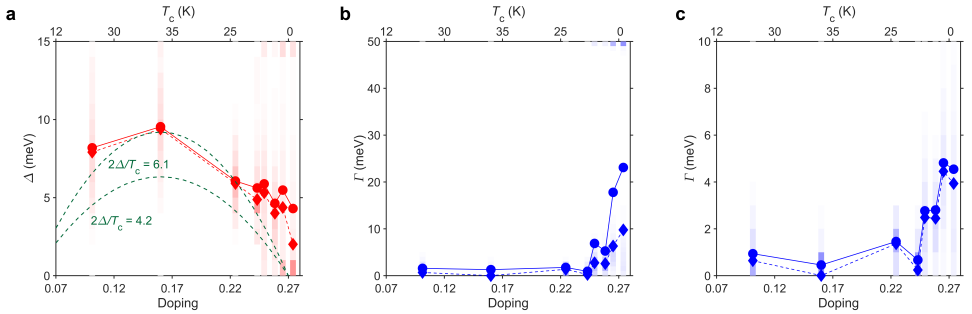

Figure A.3: The results for Δ without excluding any spectra, and for Γ including and excluding "whited-out" spectra are summarized (a, b, c respectively). The circles indicate the mean Δ, Γ for each sample, with the diamonds indicating the medians. The shaded areas in the background represent the spread in values these parameters have. The green dashed lines in the left figure indicate the behavior expected for Δ proportional to Tc. The value of 2Δ/Tc corresponds to the dirty d-wave BCS limit, while 2Δ/Tc is chosen such that it matches the OPT35K data point.

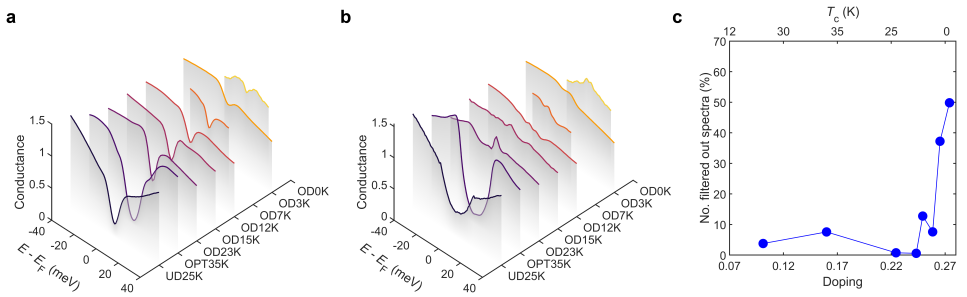

Figure A.4: a) The spatially-averaged spectra after the "whited-out" spectra have been removed. b) Spatial averages of the "whited-out" spectra for each doping level. c) The proportions of "whited-out" spectra that make up each sample as a function of doping.

A.2.3 Fit parameters figure 2.2c

Sample	Spectrum	Δ (meV)	Γ (meV)
OD23K	1	6.3 ± 1.3	1.6 ± 0.7
	2	5.4 ± 1.3	2.1 ± 0.9
	3	6.7 ± 0.8	1.1 ± 0.4
	4	6.3 ± 0.5	0.9 ± 0.3
	5	9.9 ± 1.9	2.0 ± 0.5
OD12K	1	$0.8 \pm 2E^{5}$*	$47 \pm 5E^{6}$*
	2	6.9 ± 2.0	3.0 ± 1.0
	3	3.4 ± 0.8	1.1 ± 0.8
	4	2.7 ± 0.7	0.9 ± 0.7
	5	4.2 ± 1.7	2.9 ± 1.6
OD3K	1	6.7 ± 1.7	3.1 ± 0.9
	2	4.7 ± 1.1	2.9 ± 0.9
	3	5.9 ± 1.4	3.2 ± 0.9
	4	4.9 ± 2.7	3.2 ± 2.1
	5	5.4 ± 1.4	2.6 ± 0.9

Table A.3: Fitted values of Δ and Γ for the example spectra shown in figure 2.2c of the main text, together with the 95% confidence interval for those values. The spectra are numbered from bottom to top. Entries marked with * belong to a spectrum that does not show a gap and therefore has ill-defined gap parameters.

In table A.3, we present the values of Δ and Γ as determined by our model for the examples shown in figure 2.2c of the main text. Also indicated are the 95% confidence intervals for those values. All confidence intervals are below the effective energy resolution of the experiment (see table A.2), with one exception. Spectrum number 1 of the OD12K sample does not show a gap, and therefore the values for Δ and Γ are ill-determined, as expressed by the confidence interval. This spectrum however also meets our conditions defined in section A.2.2. As such, the poorly determined values for Δ and Γ are a clear indication that we in those cases we are dealing with spectra for which those parameters have no physical meaning.

A.2.4 Energy range for fitting and approximations for the normal density of states

The spectra in the UD and OPT samples show clear pseudogap (PG) features, with PG sizes ranging from 20 meV to over 60 meV (see main text, figure 2.1a). Furthermore, in the OD regime, the normal-state DOS shows a peak near the Fermi level. These additional features next to the superconducting gap complicate the accurate fitting of the superconducting gap. We circumvent this complication by limiting our analysis

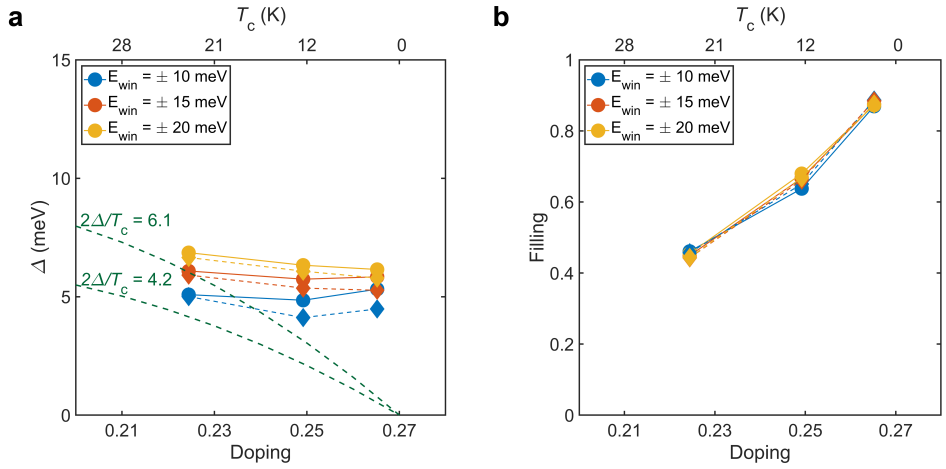

Figure A.5: Dependence of our conclusion on the choice of the energy window. The dependencies on the fitting energy window for the average Δ and filling (a, b respectively) for the overdoped samples OD23K, OD12K, and OD3K. While the absolute values of the averages vary slightly with the cutoff energy, the overall behavior of a constant gap size and increasing filling factor is independent of the cutoff.

to a small window E_{win} around the Fermi level. In this reduced energy window, the additional features are only partly visible, and can be sufficiently approximated by a polynomial DOS. The choices of E_{win} and the order of the polynomial background are arbitrary but necessary choices made before the fitting procedure. Here we show the influence the particular choices have on the superconducting gap size and filling in the OD samples.

In the main text, we use $E_{\text{win}} = \pm 15$ meV, which is a choice made before the fitting procedure. Altering this choice does not affect the main conclusions of our analysis, as shown in figure A.5. We repeat the analysis using different energy windows and find that the qualitative behavior does not change: Δ remains constant while F sharply increases in the SOD regime. Upon further increasing E_{win} beyond 20 meV, the highly inhomogeneous normal-state DOS becomes more significant, defeating the aim of focusing on the superconducting gap through an energy window. With an energy window smaller than 10 meV, we find that too little of a spectrum is left to characterize the superconducting gap accurately.

Another possible influential choice in the fitting procedure is the order of the background polynomial used to model the normal-state DOS. Figure A.6 shows the mean gap size and filling for the OD23K, OD12K, and OD3K samples for different orders of polynomial ranging from 1$^{\text{st}}$ to 4$^{\text{th}}$ order. The overall behavior of nearly constant gap size and increasing filling is present for all polynomial orders. We opt to use a 3$^{\text{rd}}$ order polynomial in the main text as it offers the best balance between underfitting and overfitting.

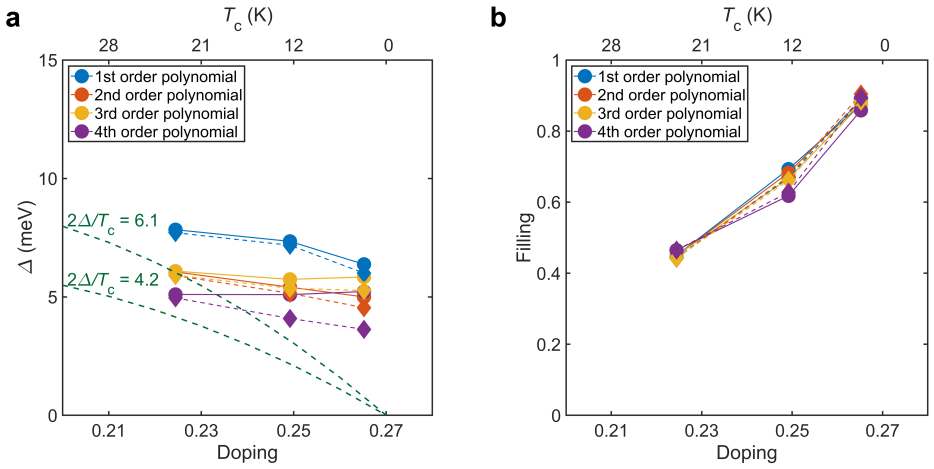

Figure A.6: Dependence of our conclusion on the choice of the polynomial normal-state DOS. The average gap size and filling (a, b) for the overdoped samples OD23K, OD12K, and OD3K as the order of the polynomial normal-state DOS is varied. While the absolute values of the averages vary a bit among the various polynomials, the overall qualitative behavior of a barely varying gap size and the drastic increasing filling is present in all cases.

A.2.5 An alternative model

Here we introduce an alternative approach to determining the gap filling, and show that the conclusions are the same using this model. We use a model which explicitly includes the filling F as a fitting parameter, in contrast to extracting F using fit parameters Δ and Γ in the main text:

$$g(E) = P(E) * [(1 - F) * \mathrm{Dynes}(\Delta, \Gamma) + F], \tag{A.2}$$

where $P(E)$ and $\mathrm{Dynes}(\Delta, \Gamma)$ are defined the same as those in the main text. The gap filling is now explicitly parametrized by the parameter F, with $F = 0$ corresponding to fully gapped and $F = 1$ to fully filled. To prevent overfitting and to limit built-in correlations between fit parameters we fix the value of Γ. Figure A.8 shows the average gap size and gap filling from the fit results using this model, analogous to figure 2.4 in the main text. For this alternative model, we exclude spectra with a) Δ close to 0 ($\Delta < 1$ meV), and b) F close to 1 ($F > 0.95$) from further analysis. In case (a) the gap sizes become smaller than our thermally limited energy resolution, preventing an accurate determination of Δ. In case (b), F becomes ill-defined as F can be absorbed into $P(E)$ when the gap is barely present. Fitting our data with this model, we find that the gap size remains constant in the OD regime, while the gap filling increases rapidly. Confirmation by an alternative model further strengthens the conclusions of the main text.

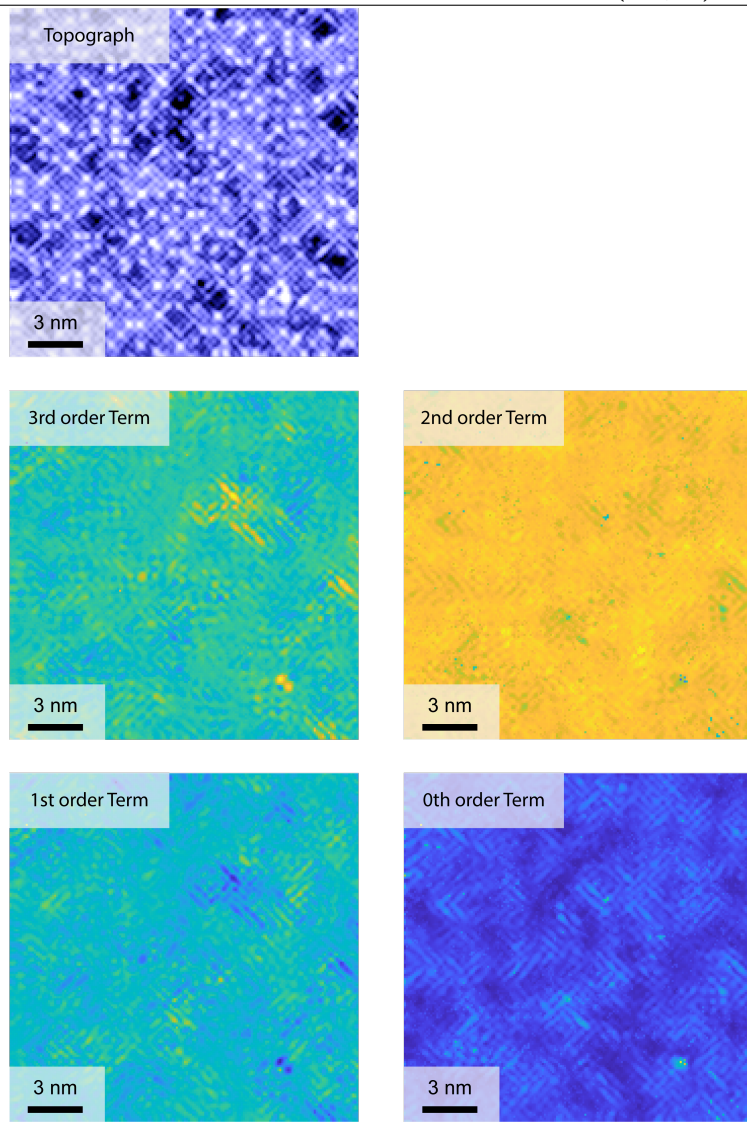

Figure A.7: Topography of the OD12K, together with the spatial distributions of the polynomial background terms used in the fits in the main text. The correlation coefficients of the 3^{rd}, 2^{nd}, and 1^{st} order terms with the topography are 0.08, -0.11, and -0.13 respectively, meaning they do not correlate with the topography. The 0^{th} order term (i.e. the constant term) does correlate with the topography (coefficient of 0.37). The underlying relation of this is that they both relate to the same quantity, the average LDOS of that spectrum. If this is low the constant background term will go down. A low average DOS also means there are less states to tunnel into with our STM tip, meaning that the tip will move closer to the sample to maintain the same setup current. Hence, this location will register as a suppression of the surface. This is clearly visible when comparing the topography with the spatial distribution of the constant background term. Darker regions of the topography are also visible as darker regions of the constant term.

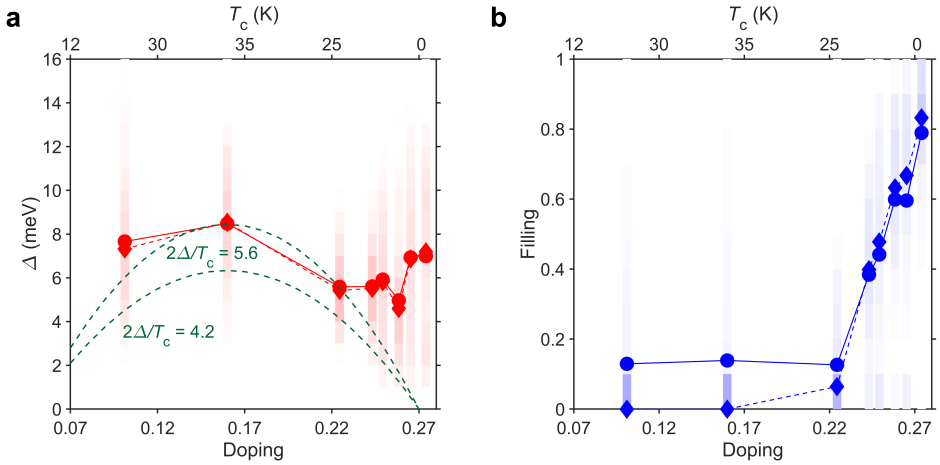

Figure A.8: Gap magnitude and filling versus doping using the alternative model The gap size (a) and the gap filling (b) as determined by the application of the alternative model described above. The shaded areas indicate the histograms of the parameters at each doping level. The average gap sizes and average filling are indicated by the circles. The median (diamonds) is shown to better reflect highly asymmetric distributions as is the case for the gap filling. The robustness of the qualitative trends against the use of different models reinforces the conclusions of the main text.

A.3 Temperature dependence

In figure A.9a, we show the temperature evolution of the average spectrum measured in the same field of view on the OD9K sample. Furthermore, we show the median values for the gap and filling parameters as a function of temperature in the same field of view in figure A.9b and A.9c, respectively. We find that a gap is still present up to 20K for the OD9K sample, even when the temperature-limited and lock-in broadened energy resolution is taken into account. With increasing temperature, we see that the gap magnitude and gap filling remain fairly constant up to 20K.

A.4 Intrinsic Metal-Induced Pair-Breaking Effects Within a Superconducting Puddle Embedded in a Metallic Matrix

In this section, we consider the case of a small d-wave superconducting puddle whose size is of the order of the superconducting coherence length ξ_0, embedded in a metallic matrix. This is a particularly relevant model for the strongly overdoped regime. Our treatment of this system is entirely mean-field; we employ large-scale numerical simulations of the Bogoliubov-de Gennes Hamiltonian to uncover interesting aspects of this system. To our knowledge, such calculations have not previously been performed in the literature; similar calculations (but for a superconducting puddle in a superconducting matrix) have been reported by Fang et al. [66] and Nunner et al [150].

We show here that one striking effect of the surrounding metallic matrix is to significantly weaken d-wave superconductivity, such that the resulting d-wave order parameter within the puddle is less than that of a bulk homogeneous system with the same pairing interaction. Decreasing the size of the puddle has the effect of decreasing the average d-wave order parameter within the puddle. We additionally find a concurrent increase in the average local density of states (LDOS) at zero energy within the puddle when the puddle size is decreased. The behavior of the puddle as its size is decreased is vastly reminiscent of the effect of increasing disorder on bulk d-wave superconductivity, and originates entirely from the mixing of the superconducting states within the puddle with the metallic states of the surrounding matrix. Thus, the surrounding metal induces pair-breaking within the puddle, very similar to the effect of disorder [151–153]. Importantly, our calculations confirm that the negative correlation between gap size and filling expected in the mean-field theory also holds for the heterogeneous case (see figure 2.4d in the main text).

In our simulations, we assume that the d-wave superconducting puddles are square patches of size $l \times l$. We self-consistently calculate the order parameter from $\Delta_{rr'} = V_{rr'}\langle c_{r\uparrow}c_{r'\downarrow}\rangle$. The pairing interaction $V_{rr'}$ is nonzero only for nearest-neighbor bonds attached to sites within the $l \times l$ patch, and otherwise vanishes. To compute $\Delta_{rr'}$ and the LDOS $\rho(r,\omega)$, we employ an exact real-space Green's function method particularly

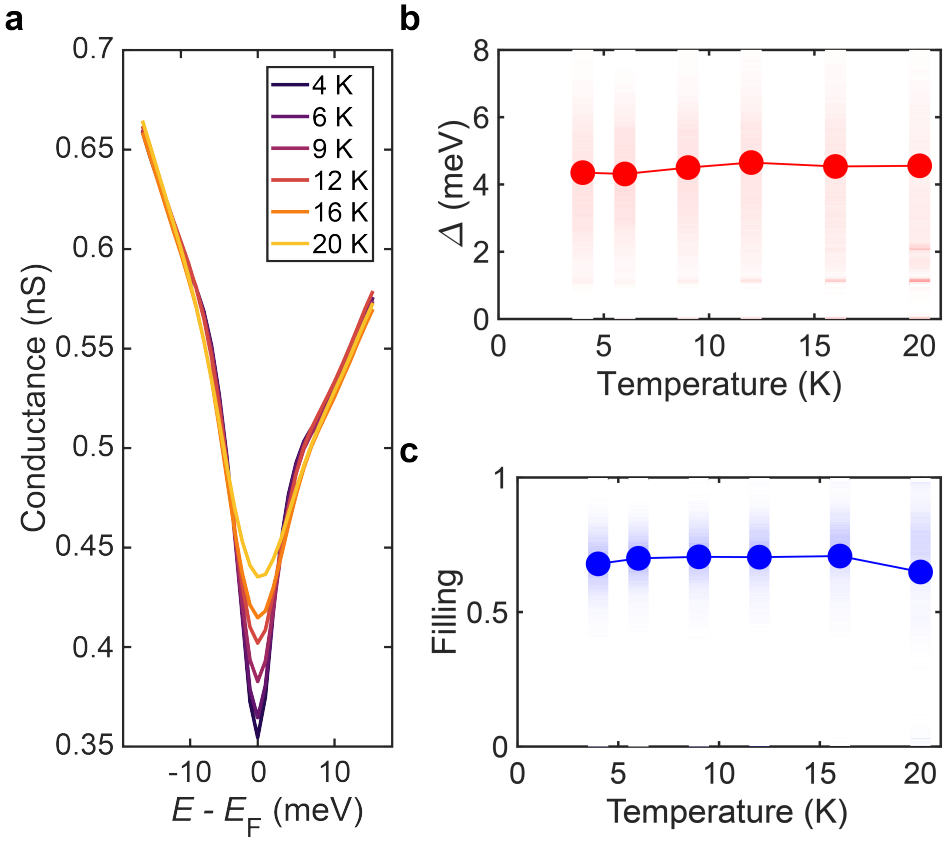

Figure A.9: Temperature evolution of the gap width and gap filling
a) Average spectra measured in the same field of view on the OD9K sample (V = -150 mV, I = -200 pA). b) Median values for the gap magnitude in the same field of view of (a), as a function of temperature. The shaded areas indicate the histograms of the gap at each temperature. c) Median values for the Filling parameter in the same field of view of (a), as a function of temperature. The shaded areas indicate the histograms of the filling at each temperature.

suited for very large inhomogeneous systems [154, 155]. For the calculations reported here, the system size is 100×200, which is larger compared to what more traditional exact-diagonalization methods can access. We iterate the calculation until the order parameter is converged, and we assume that we are at T = 0. We take the normal-state dispersion (up to next-nearest-neighbor hopping) to be given by the following parameters: $t_1 = 1, t_2 = -0.33,$ and $\mu = -1.22$ (from this point on we express all energies in units where $t_1 = 1$). The spatially resolved site-centered d-wave order parameter plotted throughout this section is obtained by adding the order parameter on all four bonds connected to a single site but assuming a sign difference between the order parameter on bonds along the x-direction and that on bonds along the y-direction.

We are interested in determining whether d-wave superconductivity in puddles behaves differently compared to the bulk case due to the abundance of low-energy states in the nearby metal, and we will tune the size of the puddles (from 5×5 to 17×17) in particular to isolate the effect of the nearby metal. One expects that the smaller the puddle, the stronger the effect of the metal, since a larger fraction of the puddle is in close proximity to the metal-superconductor boundary. We take the nearest-neighbor pairing interaction strength to be $V_0 = 1.0$ inside the superconducting puddle and $V_0 = 0$ outside it. To provide a baseline for comparisons, we perform the same calculation for a bulk d-wave superconductor as well, with the same nearest-neighbor pairing interaction $V_0 = 1.0$ present throughout the entire system. We will frequently express the puddle size in terms of l/ξ_0, where ξ_0 is the coherence length of the superconducting condensate within the puddle; this is to make clearer the effects of miniaturizing the superconducting puddle to dimensions of the order of ξ_0 itself. Note that we have suppressed here the explicit l-dependence of ξ_0, since as it turns out the magnitude of the superconducting order parameter within the puddle, and consequently ξ_0 itself, depends sensitively on l.

Our results are collected together in figure A.10. In figure A.10a, we compare the spectral gap (here rather roughly defined as half the peak-to-peak distance in energy, measured from the LDOS) to the d-wave order parameter, with both quantities averaged within the puddle. It can be seen that the spectral gap tracks the d-wave order parameter closely for the bulk system and for larger puddles (7×7 up to 17×17, all corresponding to $2 < l/\xi_0 < 10$), although for puddles the spectral gap slightly overestimates the d-wave order parameter. However, once the puddle size is small enough such that $l/\xi_0 \approx 1$ (as is the case for the 5×5 puddle), a gap is no longer visible in the spectrum, even though a nonzero superconducting order parameter remains within the puddle. The strong pair-breaking effects of the surrounding metal are most easily seen in figure A.10b. Here we plot the average d-wave order parameter within the puddle as a function of l/ξ_0. The average order parameter within all seven puddles considered is considerably less than that of the bulk system, and decreases in magnitude as l/ξ_0 is made smaller. Note that when the puddle is made smaller and smaller, the mixing of metallic states into the superconducting puddle increases since more of the puddle becomes in closer proximity with the superconductor-metal boundary, and hence there is more pair-breaking. Figure A.10c shows the average zero-energy LDOS for seven

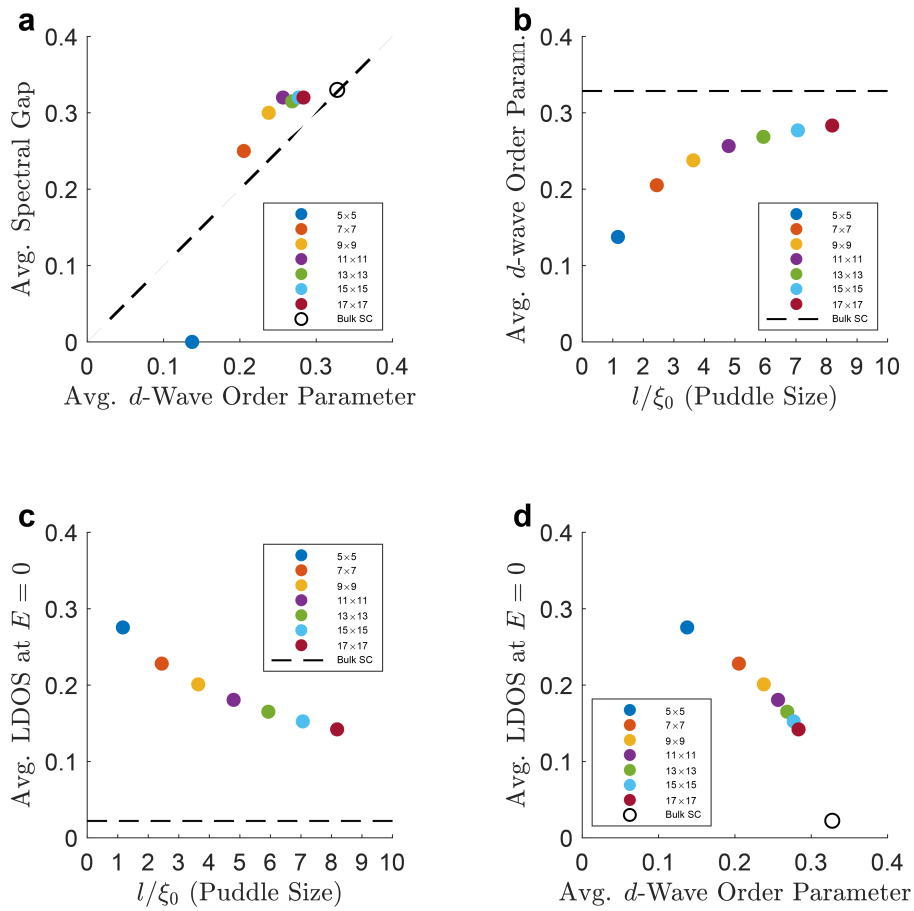

Figure A.10: Results for clean superconducting puddles within a metallic matrix of varying size, with $V_0 = 1.0$. a) plot of the average spectral gap versus the average d-wave order parameter, both averaged within the superconducting puddle, with the dashed line indicating where the two quantities are equal. It can be seen that for puddles, the spectral gap is a good indicator of the d-wave order parameter (although overestimating it, lying above the dashed line) right until the puddle becomes sufficiently small and $l/\xi_0 \approx 1$ (e.g., 5×5), at which point no gap can be seen even though a nonzero superconducting order parameter is present. b) Plot of the average of the d-wave order parameter within the superconducting puddle versus the puddle size l/ξ_0, with the value for the bulk system shown as a dashed line. c) Plot of the zero-energy LDOS averaged within the superconducting puddle versus the puddle size l/ξ_0, again with the value for the bulk system shown as a dashed line. d) Plot of the LDOS at $E = 0$ versus the d-wave order parameter, both averaged inside the superconducting puddle. Evidently, the effect of reducing the puddle size on the superconducting condensate within the puddle is the same as that of increasing the amount of disorder: the d-wave order parameter becomes smaller, while the zero-energy LDOS increases.

different puddle sizes. Notice that the zero-energy LDOS of all puddles is much bigger than that of the bulk system, and that it increases as the puddle size is decreased. As with the d-wave order parameter, the large zero-energy LDOS is an effect of the mixing of the metallic states into the superconducting puddle, giving the latter a much larger number of low-energy states than one would expect a bulk d-wave superconductor to have. The overall trend is succinctly captured by figure A.10d, which plots together with the d-wave order parameter and the zero-energy LDOS both averaged within the puddle, with the variations in both quantities due solely to the puddle size. It can be seen that these two quantities are inversely proportional to each other, with a large d-wave order parameter corresponding to a small zero-energy LDOS and vice versa. This is behavior very similar to that expected from disorder acting on a bulk d-wave superconductor; one cannot escape the conclusion that the metallic matrix induces pair-breaking effects within the superconducting puddle very similar to that of disorder.

All of these findings are more explicitly demonstrated in figure A.11, wherein we show plots of the LDOS vs. energy for three puddle sizes (5×5, 7×7, and 9×9, whose l/ξ_0 values are given approximately by 1.2, 2.4, and 3.6, respectively), in addition to the bulk d-wave case. We note first that for superconducting puddles, a striking feature of the LDOS is its very large value at $E = 0$ compared to that of the bulk system. One can also notice that for larger puddles, a gap is easily discerned in the spectrum, and coherence peaks are visible but are broader, less well-defined, and shorter in height compared to those of a bulk system. These features become progressively broader as the puddle is shrunk, and more spectral weight accumulates near the Fermi energy, a result of the fact that the average d-wave order parameter becomes smaller the tinier the puddles get. However, when the puddle is made sufficiently small such that $l/\xi_0 \approx 1$, such as the 5×5 case here, the gap ceases to be visible in the quasiparticle spectrum, and the LDOS resembles that of a normal metal. Nevertheless, there is still a nonzero d-wave order parameter present within the puddle.

In sum, we have shown here some of the surprising effects of embedding a d-wave superconducting puddle within a metallic matrix. We have demonstrated that the surrounding metallic matrix has a pair-breaking effect on the superconductivity within the puddle, akin to that of disorder, that fills the gap, including at the Fermi level. We have also shown that the smallness of the puddle has a nontrivial effect on the LDOS, with the quasiparticle spectrum within the puddle showing broad signatures of a gap that progressively becomes filled up and washed out the smaller the puddle becomes. The similarity of the pair-breaking effects of the metallic matrix to disorder points to the difficulty of attributing the effects seen in the experiment and detailed in the main text to purely mean-field effects.

Our calculations show that within a mean-field picture, pair-breaking, whether it be due to disorder or the effect of metallic states on a superconducting puddle, naturally leads to an anticorrelation between these two quantities. Such a scenario points to the necessity of "beyond-mean-field" physics in resolving the conundrum posed by the

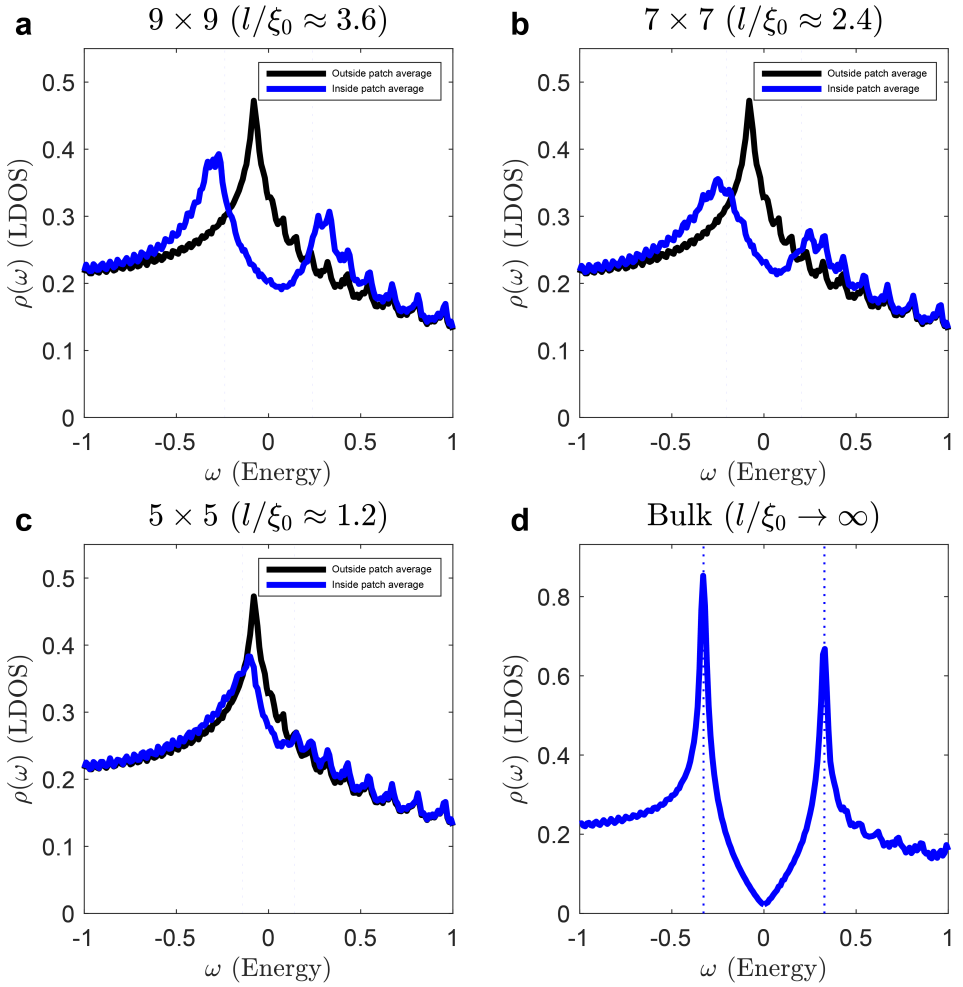

Figure A.11: Plots of the LDOS as a function of energy for a d-wave superconducting puddle inside a metallic matrix with decreasing puddle size, with $V_0 = 1.0$. The puddle sizes are 9×9, 7×7, and 5×5 (a-c), corresponding to l/ξ_0 approximately equal to 3.6, 2.4, and 1.2, respectively. Shown are LDOS averages within the puddle (blue) and outside it (black). Also shown for comparison is the average LDOS for a bulk d-wave superconductor with the same pairing interaction $V_0 = 1.0$ d) The dashed blue lines indicate the average d-wave order parameter within the superconducting puddle. Note that as the puddle size becomes smaller, the zero-energy LDOS inside the patch becomes larger, the coherence peaks become smeared out and move to lower energies, and the gap becomes less discernible.

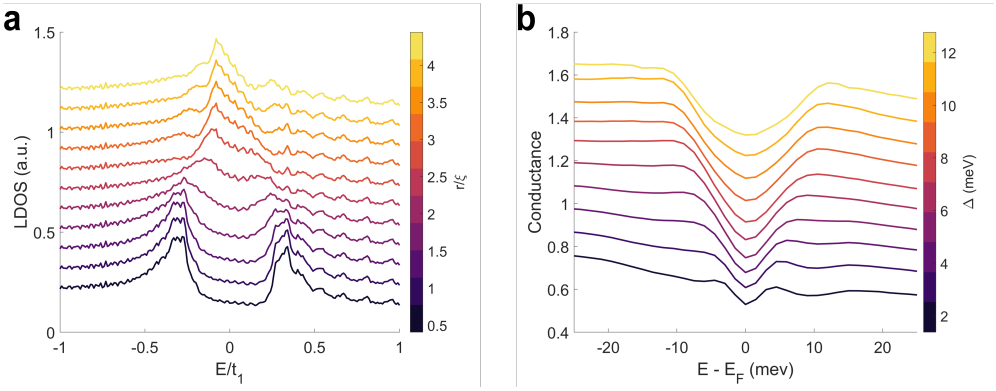

Figure A.12: a) Waterfall plot of the spectra calculated for the 9×9 puddle (the same data as presented in main text figure 2.1f), showing a clear correlation between the gap size going to zero and the coherence peaks disappearing. b) Spectra of the OD12K sample binned and averaged according to their gap size Δ, as determined by our model. The visibility of the coherence peaks here has no clear relation to the size of the gap. The spectra in (a),(b) have been shifted with respect to each other for clarity.

experimental results discussed in the main text.

A.5 Rigid band shift in overdoped Bi2201

The doping levels of the superconducting samples are determined using the Presland formula, while the doping level of the OD0K sample is extracted from the rigid band shift measured by ARPES. Below, we describe this procedure more detail.

ARPES measurements on SOD samples show a rigid band shift of the anti-nodal band bottom when the doping is increased (figure A.13). ARPES measurements were performed using the He1αline at 21.2 eV with linear polarization. The sample temperature for all samples was 50 K, and the total experimental resolution was set to 6 meV. The k-space cut was along the face of the Brillouin zone (a line spanning the direction $(\pi, \pi) - (\pi, 0) - (\pi, -\pi)$, indicated in the inset of figure A.13a).

Shown in figure A.13a as "+" symbols are the positions of the peak maxima of the Energy Distribution Curves (EDC's), extracted after dividing out the resolution broadened Fermi-Dirac distribution from the raw data. The energy position of the band bottom as shown in figure A.13b is extracted by taking the average of the EDC maxima positions within a small momentum window (indicated in figure A.13a by the two vertical red lines). Using these doping-dependent band bottom energy values, we can determine the doping level of the OD0K crystal by fitting the positions of the superconducting samples and extrapolating the result. We find that the OD0K sample has a doping level of $p = 0.274 \pm 0.008$.

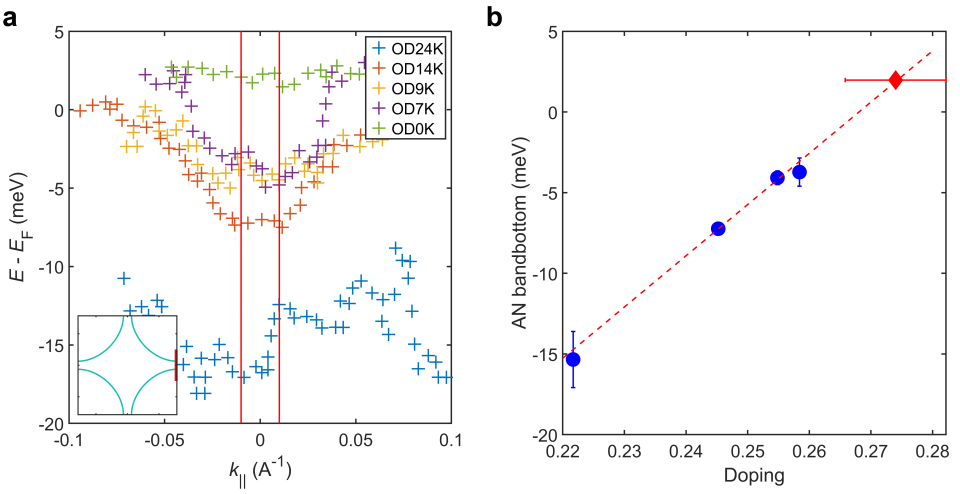

Figure A.13: Rigid band shift of the anti-nodal band bottom. The anti-nodal ARPES cut is indicated by the red line on the Fermi surface in the inset to panel (a). In (a) can be seen that the anti-nodal band bottom shifts towards the Fermi level as the samples are progressively overdoped. The energy position of the band bottom is shown in panel (b), and is given by the average position within the red vertical lines in panel (a). The red dashed line in (b) shows a fit through the band bottom energy position for the superconducting samples (blue circles). The fit is then extrapolated to determine the doping level of the non-superconducting sample (red diamond), given its measured band bottom.

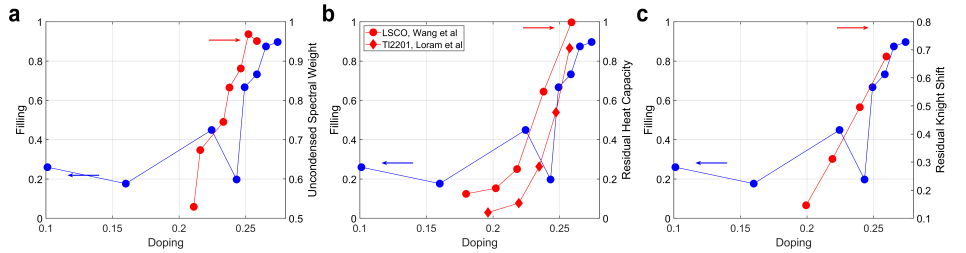

Figure A.14: a) Filling vs spectral weight from optical conductivity below Tc [40]. b) Filling vs residual specific heat [156, 157]. c) Filling vs residual Knight shift below Tc [158].

A.6 Gap filling and DOS from other experiments

Figure A.14 shows the comparison of the gap filling we observe and several other experiments determining the DOS at the Fermi level: optical conductivity [40] (figure A.14a), Specific heat measurements [156, 157] (figure A.14b), and Knight shift [158] (figure A.14c). All these probes measure a DOS at Fermi level increasing with overdoping, concomitant with the increased gap filling we observe. We posit that this increased DOS is due to increasingly more Cooper pairs broken by a non-mean field process (see main text).

A.7 Pair breaking, Gap filling and competing orders

In the overdoped cuprates several (fluctuating) orders other than superconductivity have been observed, being two distinct types of charge order and fluctuating ferromagnetism. Here we address their possible relation with our findings.
The charge order of the UD regime continues past optimal doping in the overdoped regime, weakening as the doping increases [159]. This doping dependence is opposite to the behavior of the gap filling, making this an unlikely candidate to participate in the gap filling. The second type of order, $\sqrt{2}$ order observed by STM [160]. Research on this phenomenon is ongoing – as mentioned, the relationship to RIXS data is not clear. This CDW is only visible in certain areas, and thus we deduce that it is not directly connected to the phenomenology reported here. In any case, the main points of our paper – puddle formation, persistent gap, non-mean-field breakdown – remain independent on what exactly this CDW is.

Finally, ferromagnetic fluctuations have been confirmed to exist in overdoped cuprates [161–164], but to what extend these interfere with superconductivity remains unknown. In light of the results presented in this work, one could speculate that small ferromagnetic clusters could reside in the metallic matrix. It would be these small clusters

that then give rise to the experimentally observed enhancement of the magnetic susceptibility. Note that this would not necessarily imply competition between these two phases: We observe superconducting islands embedded in a metallic matrix, but the metallic matrix itself is not necessarily caused by ferromagnetic fluctuations, but could also result from for example disorder.

Appendix B

Supplementary information to measuring local moiré lattice heterogeneity of twisted bilayer graphene

B.1 Spatial Lock-in Algorithm

B.1.1 Deformations of a lattice

We perform lock-in measurements on images that clearly display a periodic lattice. In STM, this implies we can use any topography of sufficient quality that displays the crystal lattice. The idea is to use a lock-in measurement in order to find a transformation of coordinates between the measured, "distorted" image and its pristine, undeformed equivalent (in this work, a perfect triangular lattice). Defining the measured and pristine image as $T_m(\mathbf{r}), T_r(\mathbf{r}')$ respectively, both with measurement coordinates $\mathbf{r} = (x, y) \in \mathbb{R}^2$ and lattice coordinates $\mathbf{r}' = (x', y') \in \mathbb{R}^2$, the following relation holds:

$$T_m(\mathbf{r}) = T_r\left(\mathbf{r} + \mathbf{u}(\mathbf{r})\right) = T_r\left(\mathbf{f}(\mathbf{r})\right) = T_r(\mathbf{r}') = T_m\left(\mathbf{f}^{-1}(\mathbf{r}')\right)$$

where the transformation from measurement coordinates to lattice coordinates is given by:

$$\mathbf{f}(\mathbf{r}) = \mathbf{r} + \mathbf{u}(\mathbf{r}) = \mathbf{r}' \tag{B.1}$$

Here, $\mathbf{u}(\mathbf{r})$ is called the displacement field, connecting the measurement coordinates to the lattice coordinates, as is well-established in continuum mechanics. For convenience,

A significant contribution to this appendix has been made by Tobias A. de Jong.

we also define the inverse displacement:

$$\mathbf{u}'(\mathbf{r}') := \mathbf{f}^{-1}(\mathbf{r}') - \mathbf{r}' = \mathbf{r} - \mathbf{r}'$$

Note that by substitution, we have the following relation between forward and inverse displacement:

$$\mathbf{u}'(\mathbf{r}') = \mathbf{f}^{-1}(\mathbf{f}(\mathbf{r})) - (\mathbf{r} + \mathbf{u}(\mathbf{r})) = -\mathbf{u}(\mathbf{r})$$

With this, we can express the pristine image at lattice coordinates in terms of the measured image:

$$\begin{aligned} T_r(\mathbf{r}') &= T_m\left(\mathbf{f}^{-1}(\mathbf{r}')\right) = T_m(\mathbf{r}' + \mathbf{u}'(\mathbf{r}')) \\ &= T_m\left(\mathbf{r}' - \mathbf{u}(\mathbf{r})\right) \\ &= T_m\left(\mathbf{r}' - \mathbf{u}(\mathbf{r}' - \mathbf{u}(\mathbf{r}))\right) \\ &\approx T_m\left(\mathbf{r}' - (\mathbf{u}(\mathbf{r}') - (\nabla\mathbf{u})(\mathbf{r}' - \mathbf{r}))\right) \\ &= T_m\left(\mathbf{r}' - (\mathbf{u}(\mathbf{r}') + (\nabla\mathbf{u})\mathbf{u}(\mathbf{r}))\right) \\ &= T_m\left(\mathbf{r}' - \mathbf{u}(\mathbf{r}') + (\nabla\mathbf{u})\mathbf{u}'(\mathbf{r}'))\right) \end{aligned}$$

Therefore, if we can determine $\mathbf{u}(\mathbf{r})$, and thereby $\mathbf{u}'(\mathbf{r}')$, we can reconstruct the pristine image. This is the idea of the Lawler–Fujita reconstruction algorithm [100]. In their original paper, Lawler–Fujita uses $\mathbf{u}'(\mathbf{r}') = -\mathbf{u}(\mathbf{r}')$, which is a good approximation if $\mathbf{u}$ varies slowly.

B.1.2 Properties of the deformation

The displacement field $\mathbf{u}(\mathbf{r})$ as defined above, fully describes the deformation of the lattice, but does not directly provide insight into the relevant properties. To that end, we first define the Jacobian of the transformation $\mathbf{f}$:

$$J \equiv \nabla\mathbf{f} = \mathbb{1} + \nabla\mathbf{u},$$

where $\nabla\mathbf{u}$ is the Jacobian of the displacement field, in continuum mechanics terminology the deformation gradient tensor, and in canonical terms defined as follows:

$$\nabla\mathbf{u} = \begin{pmatrix} \frac{du_x}{dx} & \frac{du_x}{dy} \\ \frac{du_y}{dx} & \frac{du_y}{dy} \end{pmatrix}$$

In order to fully characterise the deformation of the lattice, we decompose J in its polar form:

$$J = WP = WV^\top DV \ , \tag{B.2}$$

where W is the rotation matrix corresponding to the rotation of the full lattice and the matrix P describes the local anisotropy and scaling. P is further decomposed in the rotation matrix V indicating the orientation of the axis of anisotropy (i.e. the axis of largest scaling, with the axis of smallest scaling perpendicular to it) and the

diagonal scaling matrix $D = \begin{pmatrix} d_1 & 0 \\ 0 & d_2 \end{pmatrix}$, where by convention and implementation $d_1 \geq d_2$ holds for any position $\mathbf{r}$.
The geometric mean of these directional scaling factors is equal to the square root of the determinant of D and therefore of J: $\sqrt{d_1 d_2} = \sqrt{\det(J)}$. As this corresponds to the local scaling of the wavelength of the moiré lattice, we can use this to quantify the local twist angle:

$$\lambda(\mathbf{r}) = \sqrt{d_1 d_2} \frac{4\pi}{\sqrt{3}|\mathbf{q}_j|}, \tag{B.3}$$

where $|\mathbf{q}_j|$ is the length of the chosen reference vectors. This local wavelength is then converted to a local twist angle using the well-known expression:

$$\theta(\mathbf{r}) = 2 \arcsin\left(\frac{2\lambda(\mathbf{r})}{a}\right),$$

where $a = 2.46$Å is the lattice constant of graphene and $\theta(\mathbf{r})$ the local twist angle.
A quantification of the local anisotropy is given by the ratio $\kappa = d_1/d_2$ and the angle between the anisotropy axis and the x-axis is finally calculated from V: $\psi = \arctan\left(\frac{V_{xy}}{V_{xx}}\right)$.
In our practical implementation, the singular value decomposition (SVD) is used to obtain the decomposition in equation B.2 for each point in the image, and Matlab's `atan2` is used to find the right quadrant of the angles from the signs of V_{xx} and V_{xy}.

B.1.3 Determination of the displacement field $\mathbf{u}(\mathbf{r})$

In order to determine $\mathbf{u}(\mathbf{r})$ for a certain image, we perform a lock-in measurement. To clarify, we can represent any (nearly) periodic image as:

$$T_m(\mathbf{r}) = T_0 \sum_j e^{i\mathbf{q}_j \cdot (\mathbf{r} + \mathbf{u}(\mathbf{r}))} = T_0 \sum_j e^{i(\mathbf{q}_j \cdot \mathbf{r} + \phi_j)}, \tag{B.4}$$

where $\phi_j = \mathbf{q}_j \cdot \mathbf{u}(\mathbf{r})$ is the position-dependent phase of the lattice. The summation runs over the reciprocal lattice vectors $\mathbf{q}_j$ ($j \in \{1, 2, 3\}$ for a hexagonal lattice), T_0 is the constant indicating the amplitude of the modulation and $\mathbf{u}(\mathbf{r})$ is again the displacement field.
The phase is measured using standard lock-in procedure: The existing image is mixed with a reference image containing a specific plane wave. If we choose the periodicity of this reference wave sufficiently close to that of the lattice in the image itself, we can then low-pass filter the mixed image and end up with a phase map for a specific wave. For clarification:

$$\cos(\mathbf{q}_j \cdot \mathbf{r} + \phi_j) e^{-iq_j \cdot \mathbf{r}} = \frac{e^{i\phi_j}}{2} \left(1 + e^{-2i(\mathbf{q}_j \cdot \mathbf{r} + \phi_j)}\right) \mapsto \frac{1}{2} e^{i\phi_j},$$

where the cosine in the first term denotes the (real-valued) measured image, whereas the complex exponential denotes the reference wave and $\mapsto$ denotes low-pass filtering in order to get rid of the last term between brackets, corresponding to a rotating wave approximation. Alternatively, for a gaussian low-pass filter, this corresponds to a real space gaussian integration window of the lock-in.
By taking the (pointwise) angle of the complex, filtered product image, we end up with the phase map. In particular, this phase map contains information about the displacements of each pixel in the measured image $T_m(\mathbf{r})$ with respect to the pristine reference lattice $T_r(\mathbf{r})$ along the wave vector $\mathbf{q}_j$ used for the lock-in procedure. This procedure is repeated for at least one additional reciprocal lattice vector. The two phase maps are then used to find the displacement field $\mathbf{u}(\mathbf{r})$. From the definition of $\mathbf{u}(\mathbf{r})$ (eq. B.1), the following holds: $\mathbf{r}' = \mathbf{r} + \mathbf{u}(\mathbf{r})$. Multiplying this equation by the reciprocal lattice vectors, we get a system of equations expressing the projection of the distortion onto the reciprocal lattice vectors:

$$\mathbf{q}_j \cdot \mathbf{r}' = \mathbf{q}_j \cdot \mathbf{r} + \phi_j, \ j \in 1, 2, 3$$

Selecting only $j \in \{1, 2\}$, we have in matrix notation:

$$Q = \begin{pmatrix} -\mathbf{q}_1 - \\ -\mathbf{q}_2 - \end{pmatrix} = \begin{pmatrix} q_{1x} & q_{1y} \\ q_{2x} & q_{2y} \end{pmatrix},$$

such that we can write for $\phi = \binom{\phi_1}{\phi_2}$:

$$Q\mathbf{r}' = Q\mathbf{r} + \phi \ . \tag{B.5}$$

Multiplying by Q^{-1}, we find $\mathbf{r}' = \mathbf{r} + Q^{-1}\phi$, and therefore $\mathbf{u}(\mathbf{r}) = Q^{-1}\phi(\mathbf{r})$.

B.1.4 Additional notes on choice of reference vectors

Selecting two reference vectors

To obtain $\mathbf{u}(\mathbf{r})$ as described above, we only used the phase of the lock-in signal of two reference vectors. For a triangular/hexagonal lattice, *a priori* three possible choices of which two reference vectors to use are possible from the three linear independent references vectors as fitted to the FFT of the image. To select which two vectors to use for the reconstruction of $\mathbf{u}(\mathbf{r})$, we either selected the ones with the largest average lock-in amplitude, or by inspecting the phase-unwrapped images and selecting the ones where no remaining phase slips occurred.

Using more than two reference vectors

In principle, information is lost when only selecting the phase of the lock-in signal of two reference vectors to obtain $\mathbf{u}(\mathbf{r})$. Although not used in this work, in low signal-to-noise ratio situations, it could be beneficial to use all the information. Equation B.5 also holds for more than two phases and reference vectors. Although Q is not a

square matrix in this case, a solution can be obtained for each pixel using linear least squares minimization of the following equivalent equation:

$$Q\mathbf{u}(\mathbf{r}) = \phi(\mathbf{r}),$$

where additionally the amplitude of the lock-in signals can be used as weights to the minimization problem.

Isotropy

Enforcing the reference lattice to be isotropic can be done either in advance, by enforcing isotropic reference wavevectors (as applied in this work) or alternatively, after the initial lock-in step, by adding an additional linear phase $\Delta\phi_j = \mathbf{\Delta q}_j \cdot \mathbf{r}$ to the obtained phase, where $\mathbf{\Delta q}_j$ is the difference between the used reference wavevector and the isotropic wavevector.
The advantage of the latter method would be a slightly improved signal-to-noise ratio, as the smoothing window can be centered around the actual average wavevector occurring in the image instead of the ideal, equal-length, 60 degree rotated ones.

B.2 Relation of moiré lattice to relative displacement

For a non-homogeneous bilayer, the system can be fully described by two displacement fields $\mathbf{u}_\uparrow(\mathbf{r}), \mathbf{u}_\downarrow(\mathbf{r})$ of respectively the top and bottom layer compared to an undistorted system.

$$\begin{aligned} T_m(\mathbf{r}) &= T_{m\uparrow}(\mathbf{r}) \oplus T_{m\downarrow}(\mathbf{r}) \\ &= T_{r\uparrow}\left(\mathbf{r} + \mathbf{u}_\uparrow(\mathbf{r})\right) \oplus T_{r\downarrow}\left(\mathbf{r} + \mathbf{u}_\downarrow(\mathbf{r})\right) \\ &= T_{r\uparrow}\left(\mathbf{r}_\uparrow\right) \oplus T_{r\downarrow}\left(\mathbf{r}_\downarrow\right), \end{aligned}$$

where $T_r(\mathbf{r})$ denote the atomic lattices, $\mathbf{r}_\downarrow, \mathbf{r}_\uparrow$the lattice coordinates of both lattices and $\oplus$ denotes the (as of now, unspecified) operation of the combination of two lattices into one image.
We can express the deformation of one atomic lattice w.r.t the coordinates of the other:

$$\begin{aligned} T_{r\downarrow}\left(\mathbf{r}_\downarrow\right) &= T_{r\downarrow}\left(\mathbf{r} + \mathbf{u}_\downarrow(\mathbf{r})\right) = T_{r\downarrow}\left(\mathbf{f}_\downarrow(\mathbf{r})\right) \\ &= T_{r\downarrow}\left(\mathbf{f}_\downarrow(\mathbf{f}_\uparrow^{-1}(\mathbf{r}_\uparrow))\right) = T_{r\downarrow}\left(\mathbf{f}_\downarrow(\mathbf{r}_\uparrow + \mathbf{u}'_\uparrow(\mathbf{r}_\uparrow))\right) \\ &= T_{r\downarrow}\left(\mathbf{r}_\uparrow + \mathbf{u}'_\uparrow(\mathbf{r}_\uparrow) + \mathbf{u}_\downarrow(\mathbf{r}_\uparrow + \mathbf{u}'_\uparrow(\mathbf{r}_\uparrow))\right) \end{aligned}$$

Assert $\mathbf{u}_\downarrow(\mathbf{r}) = J_\downarrow\mathbf{r} + \mathbf{v}_\downarrow(\mathbf{r})$, i.e. a global rotation and/or scaling plus local variations. Note that here, $J_\downarrow$ is constant 2-by-2 matrix corresponding to a mean $\nabla\mathbf{u}$, and therefore

corresponding to $J - I$ in terms of the J defined in the previous section. In this case, we have:

$$T_{r\downarrow}(\mathbf{r}_\downarrow) = T_{r\downarrow}\left((I + J_\downarrow)(\mathbf{r}_\uparrow + \mathbf{u}'_\uparrow(\mathbf{r}_\uparrow)) + \mathbf{v}_\downarrow(\mathbf{r}_\uparrow + \mathbf{u}'_\uparrow(\mathbf{r}_\uparrow))\right)$$

For two real lattice plane waves $T_r(\mathbf{r}') = \cos(\mathbf{q}_j \cdot \mathbf{r}')$ and taking pointwise product for the $\oplus$ operator, we have:

$$\begin{aligned}
T_m(\mathbf{r}_\uparrow) &= \cos(\mathbf{q}_j \mathbf{r}_\uparrow) \cdot \\
&\quad \cos(\mathbf{q}_j \left[(I + J_\downarrow)(\mathbf{r}_\uparrow + \mathbf{u}'_\uparrow(\mathbf{r}_\uparrow)) + \mathbf{v}_\downarrow(\mathbf{r}_\uparrow + \mathbf{u}'_\uparrow(\mathbf{r}_\uparrow))\right]) \\
&= \cos(\mathbf{q}_j \mathbf{r}_\uparrow)\cos(\mathbf{q}_j \mathbf{r}_\uparrow + \delta(\mathbf{r})) \\
&= \frac{1}{2}\cos(2\mathbf{q}_j \mathbf{r}_\uparrow + \delta(\mathbf{r})) + \frac{1}{2}\cos(-\delta(\mathbf{r})) \\
&= \frac{1}{2}\cos(2\mathbf{q}_j \mathbf{r}_\uparrow + \delta(\mathbf{r})) + \frac{1}{2}\cos(+\delta(\mathbf{r}))
\end{aligned}$$

For the modulation $\delta(\mathbf{r})$ the following holds:

$$\begin{aligned}
\delta(\mathbf{r}) &= \mathbf{q}_j \left[J_\downarrow(\mathbf{r}_\uparrow + \mathbf{u}'_\uparrow(\mathbf{r}_\uparrow)) + \mathbf{u}'_\uparrow(\mathbf{r}_\uparrow) + \mathbf{v}_\downarrow(\mathbf{r}_\uparrow + \mathbf{u}'_\uparrow(\mathbf{r}_\uparrow))\right] \\
&= \mathbf{q}_j J_\downarrow \left[\mathbf{r}_\uparrow + \mathbf{u}'_\uparrow(\mathbf{r}_\uparrow) + J_\downarrow^{-1}\left(\mathbf{u}'_\uparrow(\mathbf{r}_\uparrow) + \mathbf{v}_\downarrow(\mathbf{r}_\uparrow + \mathbf{u}'_\uparrow(\mathbf{r}_\uparrow))\right)\right]
\end{aligned}$$

Substituting $\mathbf{r}_\uparrow = \mathbf{r} + \mathbf{u}_\uparrow(\mathbf{r})$ and $\mathbf{u}'_\uparrow(\mathbf{r}_\uparrow) = -\mathbf{u}_\uparrow(\mathbf{r})$:

$$\begin{aligned}
\delta(\mathbf{r}) &= \mathbf{q}_j J_\downarrow \left[\mathbf{r} - J_\downarrow^{-1}\mathbf{u}_\uparrow(\mathbf{r}) + J_\downarrow^{-1}\mathbf{v}_\downarrow(\mathbf{r})\right] \\
&= \mathbf{q}_j J_\downarrow \left[\mathbf{r} + \mathbf{u}_{moiré}(\mathbf{r})\right]
\end{aligned}$$

With $\mathbf{u}_{moiré}(\mathbf{r}) = J_\downarrow^{-1}(\mathbf{v}_\downarrow(\mathbf{r}) - \mathbf{u}_\uparrow(\mathbf{r})) = J_\downarrow^{-1}\mathbf{u}_\sim(\mathbf{r})$, where $\mathbf{u}_\sim(\mathbf{r})$ denotes the relative displacement between the upper layer and the rotated lower layer. Substituting back in T_m:

$$\begin{aligned}
T_m(\mathbf{r}) &= \frac{1}{2}\cos(2\mathbf{q}_j(\mathbf{r} + \mathbf{u}_\uparrow(\mathbf{r}) + \frac{1}{2}\left[J_\downarrow \mathbf{r} - \mathbf{u}_\uparrow(\mathbf{r}) + \mathbf{v}_\downarrow(\mathbf{r})\right])) \\
&\quad + \frac{1}{2}\cos(J_\downarrow^\top \mathbf{q}_j \left[\mathbf{r} + \mathbf{u}_{moiré}(\mathbf{r})\right]) \\
T_m(\mathbf{r}) &= \frac{1}{2}\cos(2\mathbf{q}_j(\mathbf{r} + \frac{1}{2}\left[J_\downarrow \mathbf{r} + \mathbf{u}_\uparrow(\mathbf{r}) + \mathbf{v}_\downarrow(\mathbf{r})\right])) \\
&\quad + \frac{1}{2}\cos(J_\downarrow^\top \mathbf{q}_j \left[\mathbf{r} + \mathbf{u}_{moiré}(\mathbf{r})\right])
\end{aligned}$$

Note that for a 2D lattice consisting of the sum of 2 or more cosines, each with it's own $\mathbf{q}_j$, this construction can be made for each $\mathbf{q}_j$ separately, nevertheless resulting in a single, joint $\mathbf{u}_{moiré}(\mathbf{r})$ (as expected).
For a small twist angle θ between two equal lattices, e.g. magic angle twisted bilayer graphene, we have:

$$\begin{aligned} J_\downarrow = R(\theta) - I &= \begin{pmatrix} \cos\theta - 1 & -\sin\theta \\ \sin\theta & \cos\theta - 1 \end{pmatrix} \\ &\approx \begin{pmatrix} -\frac{1}{2}\theta^2 + \frac{\theta^4}{24} & -\theta + \frac{\theta^3}{6} \\ \theta - \frac{\theta^3}{6} & -\frac{1}{2}\theta^2 + \frac{\theta^4}{24} \end{pmatrix} \\ &= \theta \begin{pmatrix} -\frac{1}{2}\theta + \frac{\theta^3}{24} & -\left(1 - \frac{\theta^2}{6}\right) \\ 1 - \frac{\theta^2}{6} & -\frac{1}{2}\theta + \frac{\theta^3}{24} \end{pmatrix} \\ &= \theta R\left(\tfrac{\pi}{2} + \tfrac{\theta}{2}\right) + \theta^3 \begin{pmatrix} \frac{\theta}{48} & -\frac{1}{3} \\ +\frac{1}{3} & \frac{\theta}{48} \end{pmatrix} \end{aligned}$$

Therefore, in this case the topography $T_m(\mathbf{r})$ consists of a sum of a cosine with approximately twice the atomic frequency and a cosine with approximately θ times the atomic frequency: the moiré frequency. As expected, this lattice is rotated by $\frac{\pi}{2}$ plus half the angle of the original rotation, i.e. angled halfway in-between both atomic lattices.

B.2.1 Relation to uniaxial strain models

Graphene has a Poisson ratio $\delta = 0.17$, so if a strain ϵ is applied in one direction, it shrinks in the perpendicular direction by $\delta\epsilon$. By applying the decomposition into $\theta(\mathbf{r})$, $\kappa(\mathbf{r})$ and $\psi(\mathbf{r})$ as described in Section B.1.1, to the relative displacement between the layers $\mathbf{u}_\sim(\mathbf{r})$ and assuming the relative strain is dominated by the strain of one layer, we can calculate that strain $\epsilon(\mathbf{r})$. For uniaxial strain, we have with these assumptions in terms of the decomposition into relative displacement:

$$\kappa(\mathbf{r}) = \frac{d_1}{d_2} = \frac{1+\epsilon}{1-\delta\epsilon},$$

and therefore we can express the strain of a single layer as follows:

$$\epsilon(\mathbf{r}) = \frac{d_1 - d_2}{d_2 + \delta d_1},$$

which can then be related to other measurements and models [90,102]. In appendix J, we discuss the accuracy of these models. Note that the measured quantity $\mathbf{u}_{moiré}(\mathbf{r})$ is related to the relative displacement by a multiplication of J^{-1}. For small twist angles, $\|J^{-1}\| \approx \frac{1}{\theta}$ (with θ in radians, i.e. for $\theta = 1.05°$ we have $\|J^{-1}\| \approx 55$), strongly amplifying effects of small relative displacement.

B.3 Phase unwrapping & singularities

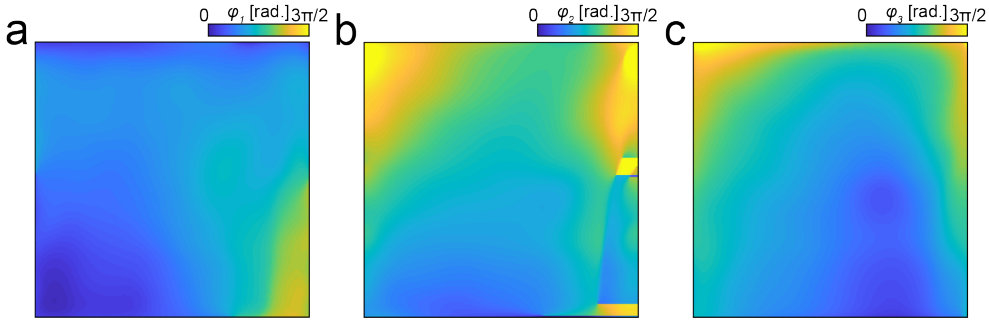

Figure B.1: Phase maps of the data shown in main text figure 3.4, and figure B.4a. a,b,c correspond to the phase maps of the Bragg peak labeled $\mathbf{q}_1$,$\mathbf{q}_2$ and $\mathbf{q}_3$ respectively (see main text figure 3.4b). Because the map corresponding to $\mathbf{q}_2$ shows some phase singularities, we use ϕ_1 and ϕ_3 for determining the displacement field.

In this work, phase unwrapping of a periodic phase is needed in two separate places: unwrapping the lock-in phase $\phi_j(\mathbf{r})$ before reconstructing $\mathbf{u}(\mathbf{r})$, and to obtain a single valued anisotropy angle $\psi(\mathbf{r})$. The phase is unwrapped in both directions of the image. The order in which this is done usually does not matter, provided there are no phase singularities present in the image. We occasionally encountered some phase singularities in one of the three phase maps (figure B.1), but we worked around this simply by using the other two phase maps in order to find the displacement field.

In case this is not an option, for example when applying this technique to a square lattice, and/or when phase slips are present in all phase maps, there are more sophisticated algorithms for phase unwrapping available: [99, 165, 166].
Some of these phaseslips were present in the $\psi(\mathbf{r})$ maps, for example the one displayed in the main text, figure 4e. Here, we used a Matlab implementation of a least-squares based phase unwrapping algorithm [165, 167].

B.4 Device overview

A schematic of the devices studied in this work is presented in figure B.2. More information about the actual fabrication process can be found in the main text.

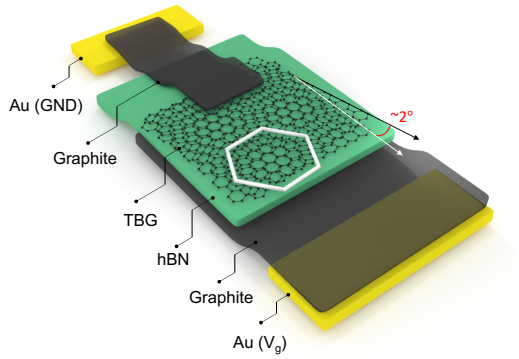

Figure B.2: Schematic overview of the devices studied in this work.

B.5 Accuracy of the algorithm

As an additional consistency check, we used the Lawler–Fujita algorithm to reconstruct the undistorted image [100], and then applied the algorithm on the undistorted image in order to extract the residual displacement field and compare it to the previously extracted displacement field. Here, a perfectly performing and consistent algorithm would extract a zero residual displacement field. Therefore, this gives an indication of the error of the quantities extracted by the algorithm. Since we decompose the displacement field, for an almost zero displacement field, we expect the effective twist angle map to become more centered around the average twist angle (in this case, 2.02°). Furthermore, we expected that most of the anisotropy is gone i.e., $\kappa \to 1$ and $\epsilon \to 0$.

We check this using the topography presented in the main text (figure 3.4) and in figure B.4a, and show the results in figure B.3. Aside from edge effects in the corner, both the residual anisotropy and the residual variations in the twist angle are more than an order of magnitude smaller than the originally obtained values, indicating self-consistency of the algorithm.

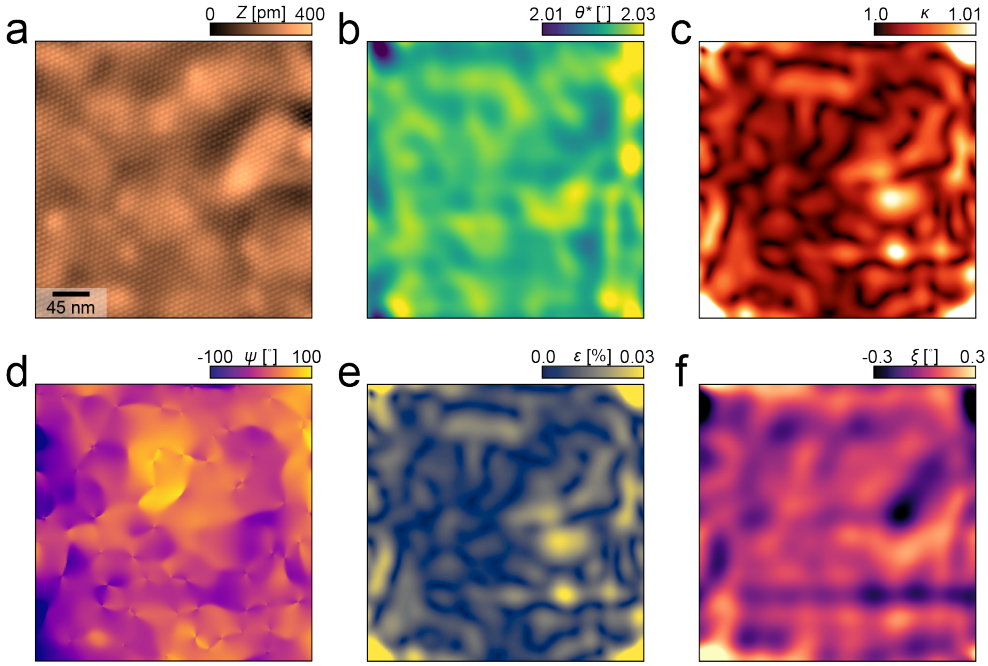

Figure B.3: a) Lawler–Fujita corrected STM topography of figure B.4a (and main text figure 3.4a). b) Extracted effective twist angle map of a. c) Extracted residual local anisotropy map of a. d) Local anisotropy angle of c. e) Heterostrain map of a. f) Local moiré rotation of a. This angle corresponds to the angle in the W matrix (equation B.2).

B.6 Validity check with more data

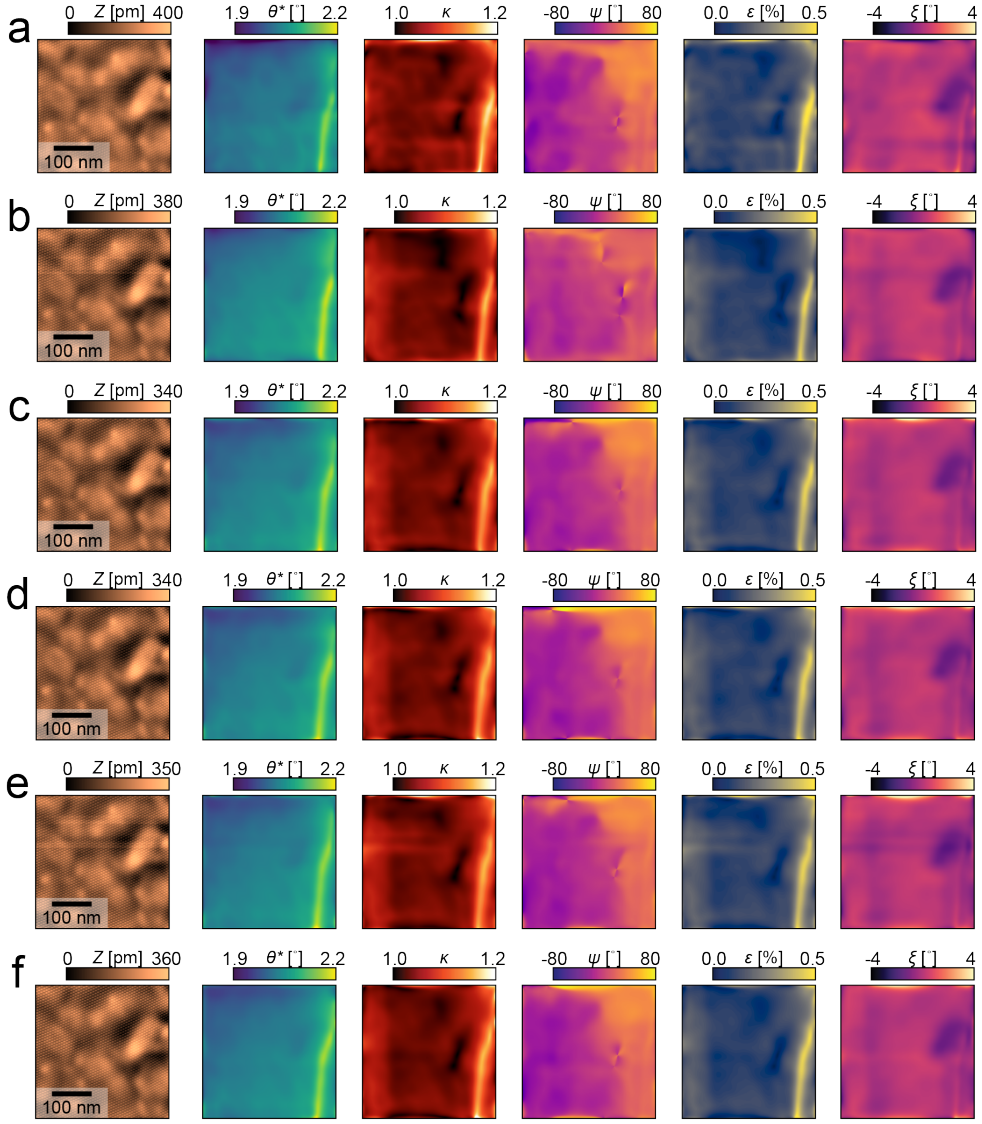

Figure B.4: Spatial lock-in output for sequentially measured topographies in the same field of view. Figure f was measured at 65 nm/s, whereas a-e were measured with a scan speed of 54 nm/s. The setup condition was kept constant between measurements: V = 250 mV, I = 20 pA.

In this work, we claim that the contribution of piezo drift to the output of our algorithm is negligible. To verify this, we apply it to multiple topographies, all se-

quentially measured on the same area. All of them are measured with a scan speed of 54 nm/s, except the last one (figure B.4f), which is measured at 65 nm/s. Because piezo drift changes with time and scan speed, comparing these datasets provides us with insight to which degree the algorithm output is affected by this effect.
The algorithm output for these measurements is displayed in figure B.4, where Figure B.4a corresponds to the data shown in the main text. For completeness, we also show $\xi(\mathbf{r})$, the angle corresponding to the matrix W (see section B.1.1).
Comparing these results from different scans, we observe that almost all deformations are reproduced, in particular the vertical line-like feature on the right and the two minima in $\kappa(\mathbf{r})$. The only features not reproduced are horizontal 'creases', corresponding to line-to-line scan artefacts. Additionally, no significant difference is observed for figure B.4f with the deviating scan speed compared to the rest. From this, we conclude that most observed deformations are intrinsic to the sample.

B.7 Heterogeneity comparison with other devices and data overview

We measured 2 additional devices, with average twist angles of 2.16° and 2.01°. The output of the spatial lock-in algorithm for these topographies is displayed in figure B.5 and figure B.6. Calculating the standard deviation for the twist angle maps, we find 0.03° and 0.06° respectively, which is consistent with the result presented in the main text.

In total, topographies from 3 different devices are presented in this work. We give a short overview of the data measured per device, and the number of pixels for each measurement in table B.1

Device	Figure	# pixels
1	3.2a	321×321
2	3.2c, 3.4, B.3 , B.4a, B.7	246×246
2	B.4b-f	984×984
2*	B.6	256×256
3	B.5	236×236

Table B.1: Overview of the measured data per device.
*: Measured after moving a few micrometer from the initial field of view.

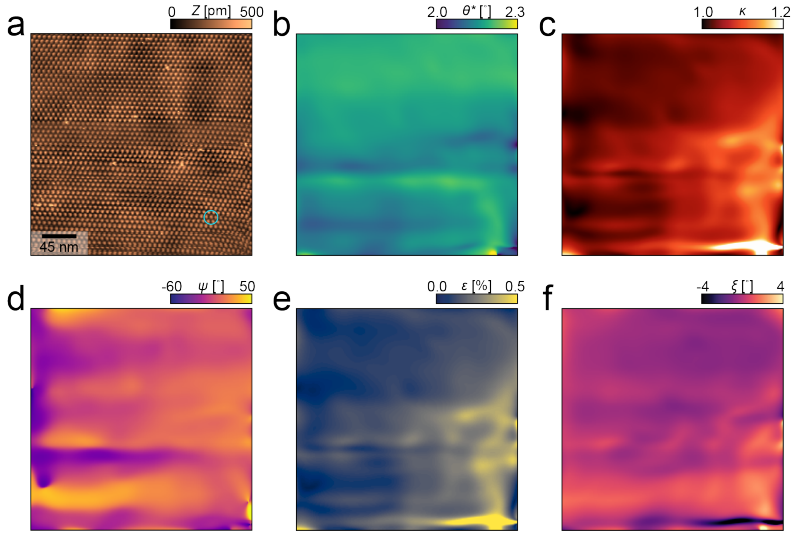

Figure B.5: a) STM topography of a TBG device with an average twist angle of 2.16° (set-up conditions: V = 170 mV, I = 20 pA). b) Extracted effective twist angle map of a. c) Extracted local anisotropy map of a. d) Local anisotropy angle of c. e) Heterostrain map of a. f) Local moiré rotation of a. This angle corresponds to the angle in the W matrix (equation B.2).

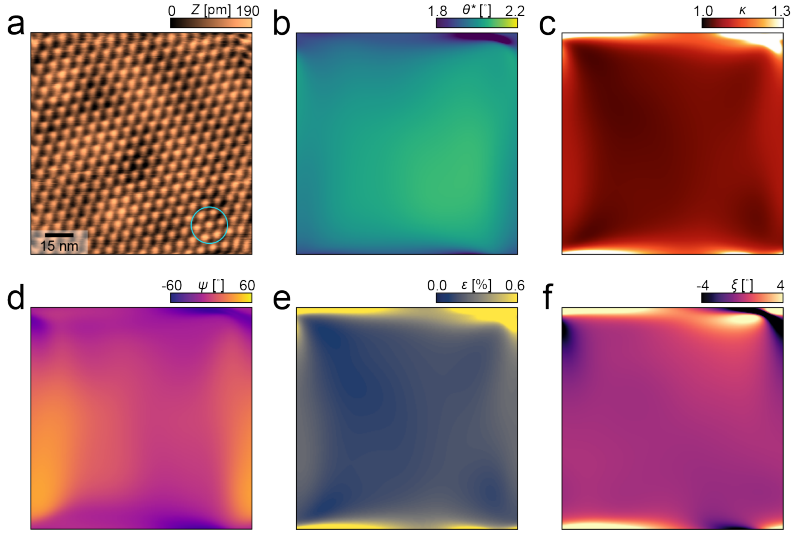

Figure B.6: a) STM topography of a TBG device with an average twist angle of 2.01° (set-up conditions: V = 350 mV, I = 100 pA). b) Extracted effective twist angle map of a. c) Extracted local anisotropy map of a. d) Local anisotropy angle of c. e) Heterostrain map of a. f) Local moiré rotation of a. This angle corresponds to the angle in the W matrix (equation B.2).

B.8 Homogeneity quantification

In the main text, the average, standard deviation and peak to peak spread are given for a cropped area of the twist angle map displayed in figure 3.4c. We find an average twist angle of 2.02° with a standard deviation of 0.02° and a peak to peak variation of 0.08°. In figure B.7, we show the topography, along with the extracted twist angle map and the crop over which these values are calculated.

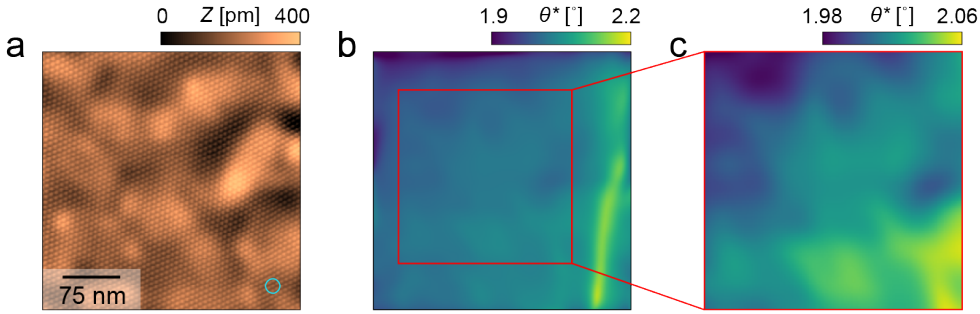

Figure B.7: a) STM topography of a device with an average twist angle of 2.02° (V = 250 mV, I = 20 pA, same data as main text figure 3.4a. b) Effective twist angle map extracted from a, by the algorithm discussed. The red square indicates the area over which the average twist angle and standard deviation are calculated. c) Effective twist angle map corresponding to the area marked by the red square in b.

Another thing to consider here is some border effects that appear in our data. Because our method is based on lock-in techniques and the real space resolution is determined by the size of the filter we choose (see main text), we can expect an area around the border of our images to be affected by artifacts. We consider the size of this border to be about two times the radius of the filter used for the spatial lock-in procedure, motivated by the Gaussian profile of the filter: Two times the sigma of a Gaussian covers roughly 95% of the weight of the window. In figure B.8, we show the extracted twist angle map, the local anisotropy and the heterostrain map of figure 3.4a in the main text, accompanied by histograms of each map both including and excluding the border.

B.9 Artificial resolution limitation for comparison with SOT

In order to compare our results with the result about twist angle homogeneity obtained on encapsulated device from SQUID-on-Tip (SOT) measurements [83], we have to consider the resolution of SOT (∼30 nm). To this end, we smear our obtained twist angle map (main text, figure 3.4c) with a Gaussian filter with a width of $\sigma = 15$ nm,

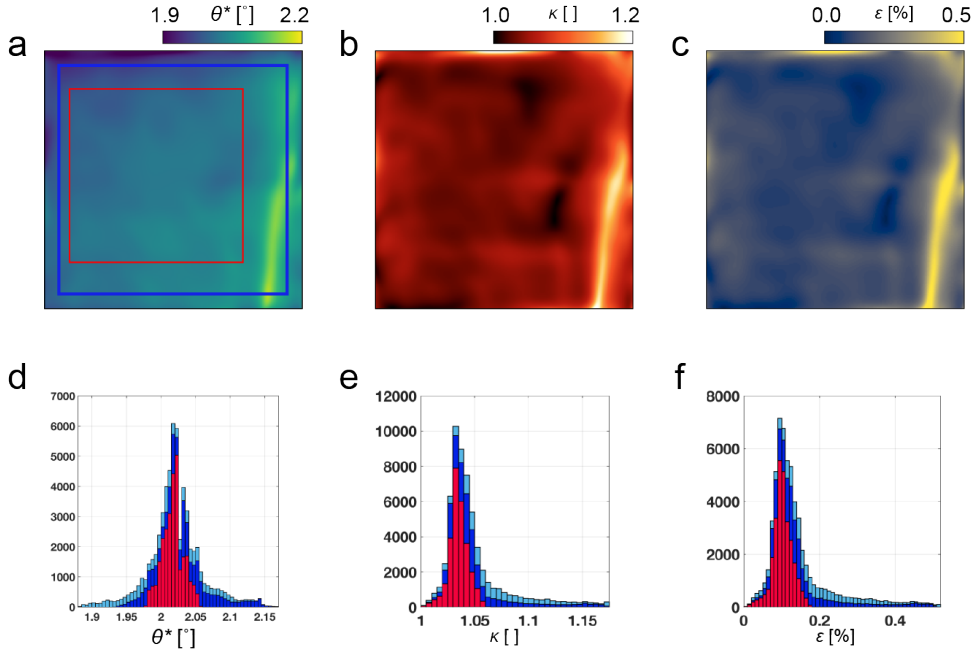

Figure B.8: a) Effective twist angle map extracted from the data shown in the main text, figure 3.4a. b) Local moiré anisotropy map $\kappa(\mathbf{r})$ extracted from the data shown in the main text, figure 3.4a. c) Heterostrain map extracted from the data shown in the main text, figure 3.4a. d-f) Histograms of the maps displayed above. The light blue histograms count the full data as shown, whereas the dark blue histograms exclude a border of two times the filter radius used in the lock-in procedure (pixels outside of the dark blue border in a). Finally, the red histograms count the data inside the area marked by the red square in a

the result of which is shown in figure B.9. Then, we obtain a peak to peak value of 0.20° and a standard deviation of 0.036°.

B.10 Error estimation of the heterostrain model

In previous STM work, the twist angle of twisted bilayer graphene has been extracted with a heterostrain model [90]. This model relies heavily on accurately fitting a Gaussian to the moiré lattice sites in order to extract their position in space, and thereby, the relative distance between neighboring sites. Here, a Gaussian is fitted to a representative example of the moiré sites in our data and we calculate the 95% confidence interval. The result is shown in figure B.10. We find a diameter of ∼1 nm for the 95% confidence interval.

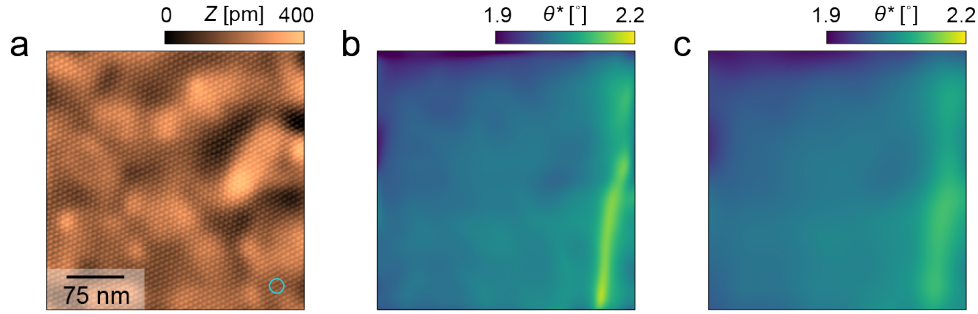

Figure B.9: a) STM topography of a device with an average twist angle of 2.02° (V = 250 mV, I = 20 pA, same data as main text figure 3.4a. b) Effective twist angle map extracted from a, by the algorithm discussed. c) Twist angle map of b after smearing with a Gaussian filter with a sigma of 15 nm.

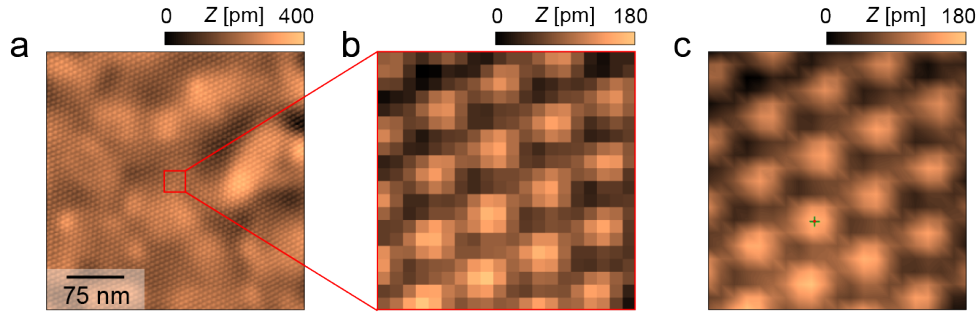

Figure B.10: a) STM topography of a device with an average twist angle of 2.02° (V = 250 mV, I = 20 pA, same data as main text figure 3.4a. b) Zoom in of a. c) Same figure as b, but plotted with interpolative shading. The red marker indicates the position of the Gaussian fitted to that moiré site and the green cross represents the extend 95% confidence interval.

B.11 Twist angle homogeneity overview

In this section, we provide the extracted twist angle homogeneity of each device presented in this work (table B.2).

B.12 Data processing

Regarding data pre-processing and post-processing, we made the following manipulations:

- Topographies are obtained from the measured data by subtracting a polynomial background up to 8^{th} order. It was verified that this did not significantly

Description	Average twist angle	peak-to-peak variation	standard deviation
Full field of view, figure B.8	2.02°	0.29°	0.039°
Blue area, figure B.8	2.02°	0.23°	0.033°
Red area, figure B.8	2.02°	0.08°	0.015°
Full field of view, figure B.8, after correcting PSF	2.02°	0.20°	0.036°
Full field of view, figure B.5 (Blue area equivalent)	2.16°	0.22°	0.029°
Full field of view, figure B.6 (Blue area equivalent)	2.03°	0.14°	0.029°

Table B.2: Overview of the twist angle homogeneity extracted per device.

influence the extracted displacement fields.

- The topography in figure 3.2a was additionally line subtracted.
- FFT's are calculated from the periodic part of the data, after applying the periodic + smooth decomposition algorithm [168].
- The FFT in figure 3.4b uses interpolative shading.
- The FFT in figure 3.2b is furthermore smeared with a gaussian filter (with a width of $\sigma = 0.5$ pixels).

Bibliography

[1] C. J. Chen, *Introduction to Scanning Tunneling Microscopy*, Oxford University Press, 1993.

[2] M. Tinkham, *Introduction to Superconductivity*, Dover Publications Inc., 2004.

[3] J. H. de Boer and E. J. W. Verwey, *Semi-conductors with partially and with completely filled 3d-lattice bands*, Proceedings of the Physical Society **49**, 59 (1937).

[4] N. F. Mott, *Metal-Insulator Transitions*, Taylor & Francis, London, 1990.

[5] M. Imada, A. Fujimori, and Y. Tokura, *Metal-insulator transitions*, Rev. Mod. Phys. **70**, 1039 (1998).

[6] D. I. Khomskii, *Transition Metal Compounds*, Cambridge University Press, 2014.

[7] J. Hubbard and B. H. Flowers, *Electron correlations in narrow energy bands*, Proceedings of the Royal Society of London **276**, 238 (1963).

[8] J. Zaanen, *Watching Rush Hour in the World of Electrons*, Science **315**, 1372 (2007).

[9] B. Keimer, S. A. Kivelson, M. R. Norman, S. Uchida, and J. Zaanen, *From quantum matter to high-temperature superconductivity in copper oxides*, Nature **518**, 179 (2015).

[10] K. Bu, W. Zhang, Y. Fei, Z. Wu, Y. Zheng, J. Gao, X. Luo, Y. Sun, and Y. Yin, *Possible strain induced Mott gap collapse in 1T-TaS_2*, Communications Physics **2**, 146 (2019).

[11] K. Yoshimatsu, H. Okabe, T. Oshima, S. Ueda, and A. Ohtomo, *Strain-induced metal-insulator transition in t_{2g} electron system of perovskite titanate $Sm_{0.5}Ca_{0.5}TiO_3$ films*, Phys. Rev. B **93**, 195159 (2016).

[12] Y. Singh and P. Gegenwart, *Antiferromagnetic Mott insulating state in single crystals of the honeycomb lattice material Na_2IrO_3*, Phys. Rev. B **82**, 064412 (2010).

[13] D. Hirai, A. Koda, A. Matsuo, K. Kindo, T. Yajima, and Z. Hiroi, *Muon Spin Rotation, High-Field Magnetization, and Structural Study on a Spin-Orbit-Entangled Mott Insulator Ba_2MgReO_6*, Journal of the Physical Society of Japan **30**, 011143 (2020).

[14] F. Ye, S. Chi, B. C. Chakoumakos, J. A. Fernandez-Baca, T. Qi, and G. Cao, *Magnetic and crystal structures of Sr_2IrO_4: A neutron diffraction study*, Phys. Rev. B **87**, 140406 (2013).

[15] C. Dhital, T. Hogan, Z. Yamani, C. de la Cruz, X. Chen, S. Khadka, Z. Ren, and S. D. Wilson, *Neutron scattering study of correlated phase behavior in Sr_2IrO_4*, Phys. Rev. B **87**, 144405 (2013).

[16] A. Schilling, M. Cantoni, J. D. Guo, and H. R. Ott, *Superconductivity above 130 K in the Hg–Ba–Ca–Cu–O system*, Nature **363**, 56 (1993).

[17] J. Bardeen, L. N. Cooper, and J. R. Schrieffer, *Microscopic Theory of Superconductivity*, Phys. Rev. **106**, 162 (1957).

[18] J. Bardeen, L. N. Cooper, and J. R. Schrieffer, *Theory of Superconductivity*, Phys. Rev. **108**, 1175 (1957).

[19] S. M. O'Mahony, W. Ren, W. Chen, Y. Chong, X. Liu, H. Eisaki, S. Uchida, M. H. Hamidian, and J. C. S. Davis, *On the electron pairing mechanism of copper-oxide high temperature superconductivity*, Proceedings of the National Academy of Sciences **119**, e2207449119 (2022).

[20] Y. Cao, V. Fatemi, A. Demir, S. Fang, S. L. Tomarken, J. Y. Luo, J. D. Sanchez-Yamagishi, K. Watanabe, T. Taniguchi, E. Kaxiras, R. C. Ashoori, and P. Jarillo-Herrero, *Correlated insulator behaviour at half-filling in magic-angle graphene superlattices*, Nature **556**, 80 (2018).

[21] Y. Cao, V. Fatemi, S. Fang, K. Watanabe, T. Taniguchi, E. Kaxiras, and P. Jarillo-Herrero, *Unconventional superconductivity in magic-angle graphene superlattices*, Nature **556**, 43 (2018).

[22] R. Bistritzer and A. H. MacDonald, *Moiré bands in twisted double-layer graphene*, Proceedings of the National Academy of Sciences **108**, 12233 (2011).

[23] G. Li, A. Luican, J. M. B. Lopes dos Santos, A. H. Castro Neto, A. Reina, J. Kong, and E. Y. Andrei, *Observation of Van Hove singularities in twisted graphene layers*, Nature Physics **6**, 109 (2010).

[24] S. Lisi et al., *Observation of flat bands in twisted bilayer graphene*, Nature Physics **17**, 189 (2021).

[25] E. Y. Andrei and A. H. MacDonald, *Graphene bilayers with a twist*, Nature Materials **19**, 1265 (2020).

[26] B. J. Kim, H. Jin, S. J. Moon, J.-Y. Kim, B.-G. Park, C. S. Leem, J. Yu, T. W. Noh, C. Kim, S.-J. Oh, J.-H. Park, V. Durairaj, G. Cao, and E. Rotenberg, *Novel $J_{\text{eff}} = 1/2$ Mott State Induced by Relativistic Spin-Orbit Coupling in Sr_2IrO_4*, Phys. Rev. Lett. **101**, 076402 (2008).

[27] G. Cao and P. Schlottmann, *The challenge of spin–orbit-tuned ground states in iridates: a key issues review*, Reports on Progress in Physics **81**, 042502 (2018).

[28] I. Božović, X. He, J. Wu, and A. T. Bollinger, *Dependence of the critical temperature in overdoped copper oxides on superfluid density*, Nature **536**, 309 (2016).

[29] Y. J. Uemura, A. Keren, L. P. Le, G. M. Luke, W. D. Wu, Y. Kubo, T. Manako, Y. Shimakawa, M. Subramanian, J. L. Cobb, and J. T. Markert, *Magnetic-field penetration depth in $Tl_2Ba_2CuO_{6+\delta}$ in the overdoped regime*, Nature **364**, 605 (1993).

[30] T. R. Lemberger, I. Hetel, A. Tsukada, M. Naito, and M. Randeria, *Superconductor-to-metal quantum phase transition in overdoped $La_{2-x}Sr_xCuO_4$*, Phys. Rev. B **83**, 140507 (2011).

[31] N. R. Lee-Hone, J. S. Dodge, and D. M. Broun, *Disorder and superfluid density in overdoped cuprate superconductors*, Phys. Rev. B **96**, 024501 (2017).

[32] Z.-X. Li, S. A. Kivelson, and D.-H. Lee, *Superconductor-to-metal transition in overdoped cuprates*, npj Quantum Materials **6**, 36 (2021).

[33] N. R. Lee-Hone, H. U. Özdemir, V. Mishra, D. M. Broun, and P. J. Hirschfeld, *Low energy phenomenology of the overdoped cuprates: Viability of the Landau-BCS paradigm*, Phys. Rev. Research **2**, 013228 (2020).

[34] B. Vignolle, A. Carrington, R. A. Cooper, M. M. J. French, A. P. Mackenzie, C. Jaudet, D. Vignolles, C. Proust, and N. E. Hussey, *Quantum oscillations in an overdoped high-Tc superconductor*, Nature **455**, 952 (2008).

[35] K. Fujita, C. K. Kim, I. Lee, J. Lee, M. H. Hamidian, I. A. Firmo, S. Mukhopadhyay, H. Eisaki, S. Uchida, M. J. Lawler, E.-A. Kim, and J. C. Davis, *Simultaneous Transitions in Cuprate Momentum-Space Topology and Electronic Symmetry Breaking*, Science **344**, 612 (2014).

[36] S.-D. Chen, M. Hashimoto, Y. He, D. Song, K.-J. Xu, J.-F. He, T. P. Devereaux, H. Eisaki, D.-H. Lu, J. Zaanen, and Z.-X. Shen, *Incoherent strange metal sharply bounded by a critical doping in Bi2212*, Science **366**, 1099 (2019).

[37] Y. He, M. Hashimoto, D. Song, S. D. Chen, J. He, I. M. Vishik, B. Moritz, D. H. Lee, N. Nagaosa, J. Zaanen, T. P. Devereaux, Y. Yoshida, H. Eisaki, D. H. Lu, and Z. X. Shen, *Rapid change of superconductivity and electron-phonon coupling through critical doping in Bi-2212*, Science **362**, 62 (2018).

[38] T. Valla, I. K. Drozdov, and G. D. Gu, *Disappearance of superconductivity due to vanishing coupling in the overdoped $Bi_2Sr_2CaCu_2O_{8+\delta}$*, Nature Communications **11**, 569 (2020).

[39] J. Ayres, M. Berben, M. Čulo, Y. T. Hsu, E. van Heumen, Y. Huang, J. Zaanen, T. Kondo, T. Takeuchi, J. R. Cooper, C. Putzke, S. Friedemann, A. Carrington, and N. E. Hussey, *Incoherent transport across the strange-metal regime of overdoped cuprates*, Nature **595**, 661 (2021).

[40] F. Mahmood, X. He, I. Božović, and N. P. Armitage, *Locating the Missing Superconducting Electrons in the Overdoped Cuprates $La_{2-x}Sr_xCuO_4$*, Phys. Rev. Lett. **122**, 027003 (2019).

[41] J. Zaanen, *Superconducting electrons go missing*, Nature **536**, 282 (2016).

[42] T. A. Maier, S. Karakuzu, and D. J. Scalapino, *Overdoped end of the cuprate phase diagram*, Phys. Rev. Research **2**, 033132 (2020).

[43] K. Bouadim, Y. L. Loh, M. Randeria, and N. Trivedi, *Single- and two-particle energy gaps across the disorder-driven superconductor–insulator transition*, Nature Physics **7**, 884 (2011).

[44] N. Trivedi, Y. L. Loh, K. Bouadim, and M. Randeria, *Emergent granularity and pseudogap near the superconductor-insulator transition*, **376**, 012001 (2012).

[45] B. Spivak, P. Oreto, and S. A. Kivelson, *Theory of quantum metal to superconductor transitions in highly conducting systems*, Phys. Rev. B **77**, 214523 (2008).

[46] B. Spivak, P. Oreto, and S. A. Kivelson, *d-wave to s-wave to normal metal transitions in disordered superconductors*, Physica B: Condensed Matter **404**, 462 (2009).

[47] J. F. Dodaro and S. A. Kivelson, *Generalization of Anderson's theorem for disordered superconductors*, Phys. Rev. B **98**, 174503 (2018).

[48] A. Ghosal, M. Randeria, and N. Trivedi, *Inhomogeneous pairing in highly disordered s-wave superconductors*, Phys. Rev. B **65**, 014501 (2001).

[49] A. Ghosal, M. Randeria, and N. Trivedi, *Role of Spatial Amplitude Fluctuations in Highly Disordered s-Wave Superconductors*, Phys. Rev. Lett. **81**, 3940 (1998).

[50] C. Putzke, S. Benhabib, W. Tabis, J. Ayres, Z. Wang, L. Malone, S. Licciardello, J. Lu, T. Kondo, T. Takeuchi, N. E. Hussey, J. R. Cooper, and A. Carrington, *Reduced Hall carrier density in the overdoped strange metal regime of cuprate superconductors*, Nature Physics **17**, 826 (2021).

[51] A. Piriou, N. Jenkins, C. Berthod, I. Maggio-Aprile, and Ø. Fischer, *First direct observation of the Van Hove singularity in the tunnelling spectra of cuprates*, Nature Communications **2**, 221 (2011).

[52] X. Li, Y. Ding, C. He, W. Ruan, P. Cai, C. Ye, Z. Hao, L. Zhao, X. Zhou, Q. Wang, and Y. Wang, *Quasiparticle interference and charge order in a heavily overdoped non-superconducting cuprate*, **20**, 063041 (2018).

[53] Y. He, Y. Yin, M. Zech, A. Soumyanarayanan, M. M. Yee, T. Williams, M. C. Boyer, K. Chatterjee, W. D. Wise, I. Zeljkovic, T. Kondo, T. Takeuchi, H. Ikuta, P. Mistark, R. S. Markiewicz, A. Bansil, S. Sachdev, E. W. Hudson, and J. E. Hoffman, *Fermi Surface and Pseudogap Evolution in a Cuprate Superconductor*, Science **344**, 608 (2014).

[54] Y. Fei, K. Bu, W. Zhang, Y. Zheng, X. Sun, Y. Ding, X. Zhou, and Y. Yin, *Electronic effect of doped oxygen atoms in Bi2201 superconductors determined by scanning tunneling microscopy*, Science China Physics, Mechanics & Astronomy **61**, 127404 (2018).

[55] J. W. Alldredge, J. Lee, K. McElroy, M. Wang, K. Fujita, Y. Kohsaka, C. Taylor, H. Eisaki, S. Uchida, P. J. Hirschfeld, and J. C. Davis, *Evolution of the electronic excitation spectrum with strongly diminishing hole density in superconducting* $Bi_2Sr_2CaCu_2O_{8+\delta}$, Nature Physics **4**, 319 (2008).

[56] R. C. Dynes, V. Narayanamurti, and J. P. Garno, *Direct Measurement of Quasiparticle-Lifetime Broadening in a Strong-Coupled Superconductor*, Phys. Rev. Lett. **41**, 1509 (1978).

[57] F. Herman and R. Hlubina, *Microscopic interpretation of the Dynes formula for the tunneling density of states*, Phys. Rev. B **94**, 144508 (2016).

[58] F. Herman and R. Hlubina, *Consistent two-lifetime model for spectral functions of superconductors*, Phys. Rev. B **95**, 094514 (2017).

[59] Y. Li et al., *Strongly overdoped* $La_{2-x}Sr_xCuO_4$*: Evidence for Josephson-coupled grains of strongly correlated superconductor*, Phys. Rev. B **106**, 224515 (2022).

[60] Y. Ding et al., *Disappearance of Superconductivity and a Concomitant Lifshitz Transition in Heavily Overdoped* $Bi_2Sr_2CuO_6$ *Superconductor Revealed by Angle-Resolved Photoemission Spectroscopy*, **36**, 017402 (2019).

[61] Y. He, S.-D. Chen, Z.-X. Li, D. Zhao, D. Song, Y. Yoshida, H. Eisaki, T. Wu, X.-H. Chen, D.-H. Lu, C. Meingast, T. P. Devereaux, R. J. Birgeneau, M. Hashimoto, D.-H. Lee, and Z.-X. Shen, *Superconducting Fluctuations in Overdoped* $Bi_2Sr_2CaCu_2O_{8+\delta}$, Phys. Rev. X **11**, 031068 (2021).

[62] M. Franz and A. J. Millis, *Phase fluctuations and spectral properties of underdoped cuprates*, Phys. Rev. B **58**, 14572 (1998).

[63] E. Berg and E. Altman, *Evolution of the Fermi Surface of d-Wave Superconductors in the Presence of Thermal Phase Fluctuations*, Phys. Rev. Lett. **99**, 247001 (2007).

[64] T. Kondo, Y. Hamaya, A. D. Palczewski, T. Takeuchi, J. S. Wen, Z. J. Xu, G. Gu, J. Schmalian, and A. Kaminski, *Disentangling Cooper-pair formation above the transition temperature from the pseudogap state in the cuprates*, Nature Physics **7**, 21 (2011).

[65] C. Howald, P. Fournier, and A. Kapitulnik, *Inherent inhomogeneities in tunneling spectra of $Bi_2Sr_2CaCu_2O_{8-x}$ crystals in the superconducting state*, Phys. Rev. B **64**, 100504 (2001).

[66] A. C. Fang, L. Capriotti, D. J. Scalapino, S. A. Kivelson, N. Kaneko, M. Greven, and A. Kapitulnik, *Gap-Inhomogeneity-Induced Electronic States in Superconducting $Bi_2Sr_2CaCu_2O_{8+\delta}$*, Phys. Rev. Lett. **96**, 017007 (2006).

[67] A. N. Pasupathy, A. Pushp, K. K. Gomes, C. V. Parker, J. Wen, Z. Xu, G. Gu, S. Ono, Y. Ando, and A. Yazdani, *Electronic Origin of the Inhomogeneous Pairing Interaction in the High-Tc Superconductor $Bi_2Sr_2CaCu_2O_{8+\delta}$*, Science **320**, 196 (2008).

[68] C. V. Parker, A. Pushp, A. N. Pasupathy, K. K. Gomes, J. Wen, Z. Xu, S. Ono, G. Gu, and A. Yazdani, *Nanoscale Proximity Effect in the High-Temperature Superconductor $Bi_2Sr_2CaCu_2O_{8+\delta}$ Using a Scanning Tunneling Microscope*, Phys. Rev. Lett. **104**, 117001 (2010).

[69] B. Sacépé, M. Feigel'man, and T. M. Klapwijk, *Quantum breakdown of superconductivity in low-dimensional materials*, Nature Physics **16**, 734 (2020).

[70] K. M. Bastiaans, D. Chatzopoulos, J.-F. Ge, D. Cho, W. O. Tromp, J. M. van Ruitenbeek, M. H. Fischer, P. J. de Visser, D. J. Thoen, E. F. C. Driessen, T. M. Klapwijk, and M. P. Allan, *Direct evidence for Cooper pairing without a spectral gap in a disordered superconductor above Tc*, Science **374**, 608 (2021).

[71] I. Božović and J. Levy, *Pre-formed Cooper pairs in copper oxides and $LaAlO_3$-$SrTiO_3$ heterostructures*, Nature Physics **16**, 712 (2020).

[72] K. K. Gomes, A. N. Pasupathy, A. Pushp, S. Ono, Y. Ando, and A. Yazdani, *Visualizing pair formation on the atomic scale in the high-Tc superconductor $Bi_2Sr_2CaCu_2O_{8+\delta}$*, Nature **447**, 569 (2007).

[73] M. P. Allan, M. H. Fischer, O. Ostojic, and A. Andringa, *Creating better superconductors by periodic nanopatterning*, SciPost Phys. **3**, 010 (2017).

[74] X. Lu, P. Stepanov, W. Yang, M. Xie, M. A. Aamir, I. Das, C. Urgell, K. Watanabe, T. Taniguchi, G. Zhang, A. Bachtold, A. H. MacDonald, and D. K. Efetov, *Superconductors, orbital magnets and correlated states in magic-angle bilayer graphene*, Nature **574**, 653 (2019).

[75] H. Polshyn, M. Yankowitz, S. Chen, Y. Zhang, K. Watanabe, T. Taniguchi, C. R. Dean, and A. F. Young, *Large linear-in-temperature resistivity in twisted bilayer graphene*, Nature Physics **15**, 1011 (2019).

[76] A. L. Sharpe, E. J. Fox, A. W. Barnard, J. Finney, K. Watanabe, T. Taniguchi, M. A. Kastner, and D. Goldhaber-Gordon, *Emergent ferromagnetism near three-quarters filling in twisted bilayer graphene*, Science **365**, 605 (2019).

[77] M. Yankowitz, S. Chen, H. Polshyn, Y. Zhang, K. Watanabe, T. Taniguchi, D. Graf, A. F. Young, and C. R. Dean, *Tuning superconductivity in twisted bilayer graphene*, Science **363**, 1059 (2019).

[78] P. Stepanov, I. Das, X. Lu, A. Fahimniya, K. Watanabe, T. Taniguchi, F. H. L. Koppens, J. Lischner, L. Levitov, and D. K. Efetov, *Untying the insulating and superconducting orders in magic-angle graphene*, Nature **583**, 375 (2020).

[79] E. Codecido, Q. Wang, R. Koester, S. Che, H. Tian, R. Lv, S. Tran, K. Watanabe, T. Taniguchi, F. Zhang, M. Bockrath, and C. N. Lau, *Correlated insulating and superconducting states in twisted bilayer graphene below the magic angle*, Science Advances **5**, eaaw9770 (2019).

[80] Y. Saito, J. Ge, K. Watanabe, T. Taniguchi, and A. F. Young, *Independent superconductors and correlated insulators in twisted bilayer graphene*, Nature Physics **16**, 926 (2020).

[81] Y. Cao, D. Chowdhury, D. Rodan-Legrain, O. Rubies-Bigorda, K. Watanabe, T. Taniguchi, T. Senthil, and P. Jarillo-Herrero, *Strange Metal in Magic-Angle Graphene with near Planckian Dissipation*, Phys. Rev. Lett. **124**, 076801 (2020).

[82] L. Balents, C. R. Dean, D. K. Efetov, and A. F. Young, *Superconductivity and strong correlations in moiré flat bands*, Nature Physics **16**, 725 (2020).

[83] A. Uri, S. Grover, Y. Cao, J. A. Crosse, K. Bagani, D. Rodan-Legrain, Y. Myasoedov, K. Watanabe, T. Taniguchi, P. Moon, M. Koshino, P. Jarillo-Herrero, and E. Zeldov, *Mapping the twist-angle disorder and Landau levels in magic-angle graphene*, Nature **581**, 47 (2020).

[84] I. Razado-Colambo, J. Avila, J. P. Nys, C. Chen, X. Wallart, M. C. Asensio, and D. Vignaud, *NanoARPES of twisted bilayer graphene on SiC: absence of velocity renormalization for small angles*, Scientific Reports **6**, 27261 (2016).

[85] A. J. H. Jones, R. Muzzio, P. Majchrzak, S. Pakdel, D. Curcio, K. Volckaert, D. Biswas, J. Gobbo, S. Singh, J. T. Robinson, K. Watanabe, T. Taniguchi, T. K. Kim, C. Cacho, N. Lanata, J. A. Miwa, P. Hofmann, J. Katoch, and S. Ulstrup, *Observation of Electrically Tunable van Hove Singularities in Twisted Bilayer Graphene from NanoARPES*, Advanced Materials **32**, 2001656 (2020).

[86] L. J. McGilly, A. Kerelsky, N. R. Finney, K. Shapovalov, E.-M. Shih, A. Ghiotto, Y. Zeng, S. L. Moore, W. Wu, Y. Bai, K. Watanabe, T. Taniguchi, M. Stengel, L. Zhou, J. Hone, X. Zhu, D. N. Basov, C. Dean, C. E. Dreyer, and A. N. Pasupathy, *Visualization of moiré superlattices*, Nature Nanotechnology **15**, 580 (2020).

[87] S. S. Sunku, A. S. McLeod, T. Stauber, H. Yoo, D. Halbertal, G. Ni, A. Sternbach, B.-Y. Jiang, T. Taniguchi, K. Watanabe, P. Kim, M. M. Fogler, and D. N. Basov, *Nano-photocurrent Mapping of Local Electronic Structure in Twisted Bilayer Graphene*, Nano Letters **20**, 2958 (2020).

[88] U. Zondiner, A. Rozen, D. Rodan-Legrain, Y. Cao, R. Queiroz, T. Taniguchi, K. Watanabe, Y. Oreg, F. von Oppen, A. Stern, E. Berg, P. Jarillo-Herrero, and S. Ilani, *Cascade of phase transitions and Dirac revivals in magic-angle graphene*, Nature **582**, 203 (2020).

[89] Y. Choi, J. Kemmer, Y. Peng, A. Thomson, H. Arora, R. Polski, Y. Zhang, H. Ren, J. Alicea, G. Refael, F. von Oppen, K. Watanabe, T. Taniguchi, and S. Nadj-Perge, *Electronic correlations in twisted bilayer graphene near the magic angle*, Nature Physics **15**, 1174 (2019).

[90] A. Kerelsky, L. J. McGilly, D. M. Kennes, L. Xian, M. Yankowitz, S. Chen, K. Watanabe, T. Taniguchi, J. Hone, C. Dean, A. Rubio, and A. N. Pasupathy, *Maximized electron interactions at the magic angle in twisted bilayer graphene*, Nature **572**, 95 (2019).

[91] Y. Xie, B. Lian, B. Jäck, X. Liu, C.-L. Chiu, K. Watanabe, T. Taniguchi, B. A. Bernevig, and A. Yazdani, *Spectroscopic signatures of many-body correlations in magic-angle twisted bilayer graphene*, Nature **572**, 101 (2019).

[92] D. Wong, K. P. Nuckolls, M. Oh, B. Lian, Y. Xie, S. Jeon, K. Watanabe, T. Taniguchi, B. A. Bernevig, and A. Yazdani, *Cascade of electronic transitions in magic-angle twisted bilayer graphene*, Nature **582**, 198 (2020).

[93] Y. Jiang, X. Lai, K. Watanabe, T. Taniguchi, K. Haule, J. Mao, and E. Y. Andrei, *Charge order and broken rotational symmetry in magic-angle twisted bilayer graphene*, Nature **573**, 91 (2019).

[94] K. P. Nuckolls, M. Oh, D. Wong, B. Lian, K. Watanabe, T. Taniguchi, B. A. Bernevig, and A. Yazdani, *Strongly correlated Chern insulators in magic-angle twisted bilayer graphene*, Nature **588**, 610 (2020).

[95] G. Li, A. Luican, and E. Y. Andrei, *Self-navigation of a scanning tunneling microscope tip toward a micron-sized graphene sample*, Review of Scientific Instruments **82**, 073701 (2011).

[96] M. Hÿtch, *Geometric phase analysis of high resolution electron microscope images*, Scanning Microscopy **11**, 53 (1997).

[97] Y. Zhu, C. Ophus, J. Ciston, and H. Wang, *Interface lattice displacement measurement to 1pm by geometric phase analysis on aberration-corrected HAADF STEM images*, Acta Materialia **61**, 5646 (2013).

[98] H. Zhang, Z. Liu, H. Wen, H. Xie, and C. Liu, *Subset geometric phase analysis method for deformation evaluation of HRTEM images*, Ultramicroscopy **171**, 34 (2016).

[99] Q. Kemao, *Two-dimensional windowed Fourier transform for fringe pattern analysis: Principles, applications and implementations*, Optics and Lasers in Engineering **45**, 304 (2007).

[100] M. J. Lawler, K. Fujita, J. Lee, A. R. Schmidt, Y. Kohsaka, C. K. Kim, H. Eisaki, S. Uchida, J. C. Davis, J. P. Sethna, and E.-A. Kim, *Intra-unit-cell electronic nematicity of the high-Tc copper-oxide pseudogap states*, Nature **466**, 347 (2010).

[101] J. A. Slezak, J. Lee, M. Wang, K. McElroy, K. Fujita, B. M. Andersen, P. J. Hirschfeld, H. Eisaki, S. Uchida, and J. C. Davis, *Imaging the impact on cuprate superconductivity of varying the interatomic distances within individual crystal unit cells*, Proceedings of the National Academy of Sciences **105**, 3203 (2008).

[102] Z. Bi, N. F. Q. Yuan, and L. Fu, *Designing flat bands by strain*, Phys. Rev. B **100**, 035448 (2019).

[103] C. Dutreix, H. González-Herrero, I. Brihuega, M. I. Katsnelson, C. Chapelier, and V. T. Renard, *Measuring the Berry phase of graphene from wavefront dislocations in Friedel oscillations*, Nature **574**, 219 (2019).

[104] N. N. T. Nam and M. Koshino, *Lattice relaxation and energy band modulation in twisted bilayer graphene*, Phys. Rev. B **96**, 075311 (2017).

[105] L. Balents, *General continuum model for twisted bilayer graphene and arbitrary smooth deformations*, SciPost Phys. **7**, 48 (2019).

[106] R. De-Picciotto, M. Reznikov, M. Heiblum, V. Umansky, G. Bunin, and D. Mahalu, *Direct observation of a fractional charge*, Nature **389**, 162 (1997).

[107] L. Saminadayar, D. C. Glattli, Y. Jin, and B. Etienne, *Observation of the e/3 fractionally charged laughlin quasiparticle*, Phys. Rev. Lett. **79**, 2526 (1997).

[108] Y. Ronen, Y. Cohen, J.-H. Kang, A. Haim, M.-T. Rieder, M. Heiblum, D. Mahalu, and H. Shtrikman, *Charge of a quasiparticle in a superconductor*, PNAS **113**, 1743 (2016).

[109] A. Thielmann, M. H. Hettler, J. König, and G. Schön, *Cotunneling current and shot noise in quantum dots*, Phys. Rev. Lett. **95**, 146806 (2005).

[110] E. Onac, F. Balestro, B. Trauzettel, C. F. J. Lodewijk, and L. P. Kouwenhoven, *Shot-noise detection in a carbon nanotube quantum dot*, Phys. Rev. Lett. **96**, 026803 (2006).

[111] G. Iannaccone, G. Lombardi, M. Macucci, and B. Pellegrini, *Enhanced shot noise in resonant tunneling: Theory and experiment*, Phys. Rev. Lett. **80**, 1054 (1998).

[112] S. Oberholzer, E. V. Sukhorukov, C. Strunk, C. Schönenberger, T. Heinzel, and M. Holland, *Shot noise by quantum scattering in chaotic cavities*, Phys. Rev. Lett. **86**, 2114 (2001).

[113] H. E. van den Brom and J. M. van Ruitenbeek, *Quantum suppression of shot noise in atom-size metallic contacts*, Phys. Rev. Lett. **82**, 1526 (1999).

[114] Y. M. Blanter and M. Büttiker, *Shot noise in mesoscopic conductors*, Physics Reports **336**, 1 (2000).

[115] Y. M. Blanter and M. Büttiker, *Transition from sub-Poissonian to super-Poissonian shot noise in resonant quantum wells*, Physical Rev. B **59**, 10217 (1999).

[116] U. Kemiktarak, T. Ndukum, K. C. Schwab, and K. L. Ekinci, *Radio-frequency scanning tunnelling microscopy*, Nature **450**, 85 (2007).

[117] H. Birk, M. J. M. de Jong, and C. Schönenberger, *Shot-noise suppression in the single-electron tunneling regime*, Phys. Rev. Lett. **75**, 1610 (1995).

[118] H. Birk, K. Oostveen, and C. Schönenberger, *Preamplifier for electric-current noise measurements at low temperatures*, Rev. Sci. Instrum. **67**, 2977 (1996).

[119] M. J. Rost, L. Crama, P. Schakel, E. van Tol, G. B. E. M. van Velzen-Williams, C. F. Overgauw, H. ter Horst, H. Dekker, B. Okhuijsen, M. Seynen, A. Vijftigschild, P. Han, A. J. Katan, K. Schoots, R. Schumm, W. van Loo, T. H. Oosterkamp, and J. W. M. Frenken, *Scanning probe microscopes go video rate and beyond*, Rev. Sci. Instrum. **76**, 053710 (2005).

[120] H. Mamin, H. Birk, P. Wimmer, and D. Rugar, *High-speed scanning tunneling microscopy: Principles and applications*, Journal of applied physics **75**, 161 (1994).

[121] A. Burtzlaff, A. Weismann, M. Brandbyge, and R. Berndt, *Shot noise as a probe of spin-polarized transport through single atoms*, Phys. Rev. Lett. **114**, 016602 (2015).

[122] A. Burtzlaff, N. L. Schneider, A. Weismann, and R. Berndt, *Shot noise from single atom contacts in a scanning tunneling microscope*, Surface Science **643**, 10 (2016).

[123] L. DiCarlo, Y. Zhang, D. T. McClure, C. M. Marcus, L. N. Pfeiffer, and K. W. West, *System for measuring auto-and cross correlation of current noise at low temperatures*, Rev. Sci. Instrum. **77**, 073906 (2006).

[124] T. Arakawa, Y. Nishihara, M. Maeda, S. Norimoto, and K. Kobayashi, *Cryogenic amplifier for shot noise measurement at 20 mK*, Applied Physics Letters **103**, 172104 (2013).

[125] M. Hashisaka, Y. Yamauchi, S. Nakamura, S. Kasai, K. Kobayashi, and T. Ono, *Measurement for quantum shot noise in a quantum point contact at low temperatures*, Journal of Physics: Conference Series **109**, 012013 (2008).

[126] A. M. Robinson and V. I. Talyanskii, *Cryogenic amplifier for 1 Mhz with a high input impedance using a commercial pseudomorphic high electron mobility transistor*, Rev. Sci. Instrum. **75**, 3169 (2004).

[127] Q. Dong, Y. X. Liang, D. Ferry, A. Cavanna, U. Gennser, L. Couraud, and Y. Jin, *Ultra-low noise high electron mobility transistors for high-impedance and low-frequency deep cryogenic readout electronics*, Applied Physics Letters **105**, 013504 (2014).

[128] Y. Jin, Q. Dong, U. Gennser, L. Couraud, A. Cavanna, and C. Ulysse, *Ultra-low noise CryoHEMTs for cryogenic high-impedance readout electronics: Results and applications*, 13th IEEE International Conference on Solid-State and Integrated Circuit Technology (ICSICT) **1**, 342 (2016).

[129] I. Battisti, G. Verdoes, K. van Oosten, K. M. Bastiaans, and M. P. Allan, *Definition of design guidelines, construction, and performance of an ultra-stable scanning tunneling microscope for spectroscopic imaging*, Review of Scientific Instruments **89**, 123705 (2018).

[130] F. Massee, Q. Dong, A. Cavanna, Y. Jin, and M. Aprili, *Atomic scale shot-noise using cryogenic MHz circuitry*, Rev. Sci. Instrum. **89**, 093708 (2018).

[131] S. Loth, M. Etzkorn, C. P. Lutz, D. M. Eigler, and A. J. Heinrich, *Measurement of fast electron spin relaxation times with atomic resolution*, Science **329**, 1628 (2010).

[132] S. Baumann, W. Paul, T. Choi, C. P. Lutz, A. Ardavan, and A. J. Heinrich, *Electron paramagnetic resonance of individual atoms on a surface*, Science **350**, 417 (2015).

[133] M. Leeuwenhoek, R. A. Norte, K. M. Bastiaans, D. Cho, I. Battisti, Y. M. Blanter, S. Gröblacher, and M. P. Allan, *Nanofabricated tips for device-based scanning tunneling microscopy*, **30**, 335702 (2019).

[134] H. Grabert, *Dynamical Coulomb blockade of tunnel junctions driven by alternating voltages*, Phys. Rev. B **92**, 245433 (2015).

[135] I. Battisti, K. M. Bastiaans, V. Fedoseev, A. de la Torre, N. Iliopoulos, A. Tamai, E. C. Hunter, R. S. Perry, J. Zaanen, F. Baumberger, and M. P. Allan, *Universality of pseudogap and emergent order in lightly doped Mott insulators*, Nature Physics **13**, 21 (2017).

[136] T. Han, D. Liang, Y. Wang, J. Yang, H. Han, J. Wang, J. Gong, L. Luo, W. K. Zhu, C. Zhang, and Y. Zhang, *A Comparison Study of the Effects of Ba and La Doping in Sr_2IrO_4: Ir–O–Ir Bond Angle and Carrier Concentration*, Journal of Superconductivity and Novel Magnetism **30**, 3493 (2017).

[137] K. M. Bastiaans, D. Chatzopoulos, J.-F. Ge, D. Cho, W. O. Tromp, J. M. van Ruitenbeek, M. H. Fischer, P. J. de Visser, D. J. Thoen, E. F. C. Driessen, T. M. Klapwijk, and M. P. Allan, *Direct evidence for Cooper pairing without a spectral gap in a disordered superconductor above Tc*, Science **374**, 608 (2021).

[138] K. M. Bastiaans, T. Benschop, D. Chatzopoulos, D. Cho, Q. Dong, Y. Jin, and M. P. Allan, *Amplifier for scanning tunneling microscopy at MHz frequencies*, Review of Scientific Instruments **89**, 093709 (2018).

[139] I. Battisti, V. Fedoseev, K. M. Bastiaans, A. de la Torre, R. S. Perry, F. Baumberger, and M. P. Allan, *Poor electronic screening in lightly doped Mott insulators observed with scanning tunneling microscopy*, Phys. Rev. B **95**, 235141 (2017).

[140] R. M. Feenstra, Y. Dong, M. P. Semtsiv, and W. T. Masselink, *Influence of tip-induced band bending on tunnelling spectra of semiconductor surfaces*, Nanotechnology **18**, 044015 (2007).

[141] V. W. Brar, R. Decker, H.-M. Solowan, Y. Wang, L. Maserati, K. T. Chan, H. Lee, Ç. O. Girit, A. Zettl, S. G. Louie, M. L. Cohen, and M. F. Crommie, *Gate-controlled ionization and screening of cobalt adatoms on a graphene surface*, Nature Physics **7**, 43 (2011).

[142] F. Massee, Y. K. Huang, M. S. Golden, and M. Aprili, *Noisy defects in the high-Tc superconductor $Bi_2Sr_2CaCu_2O_{8+x}$*, Nature Communications **10**, 544 (2019).

[143] L. Desvignes, V. S. Stolyarov, M. Aprili, and F. Massee, *Tunable High Speed Atomic Rotor in Bi_2Se_3 Revealed by Current Noise*, ACS Nano **15**, 1421 (2021).

[144] L. Liu, L. Xiang, H. Guo, J. Wei, D. L. Li, Z. H. Yuan, J. F. Feng, X. F. Han, and J. M. D. Coey, *Low frequency noise peak near magnon emission energy in magnetic tunnel junctions*, AIP Advances **4**, 127102 (2014).

[145] S. Machlup, *Noise in Semiconductors: Spectrum of a Two-Parameter Random Signal*, Journal of Applied Physics **25**, 341 (1954).

[146] K. M. Bastiaans, D. Cho, T. Benschop, I. Battisti, Y. Huang, M. S. Golden, Q. Dong, Y. Jin, J. Zaanen, and M. P. Allan, *Charge trapping and super-Poissonian noise centres in a cuprate superconductor*, Nature Physics **14**, 1183 (2018).

[147] C. H. Sohn, M.-C. Lee, H. J. Park, K. J. Noh, H. K. Yoo, S. J. Moon, K. W. Kim, T. F. Qi, G. Cao, D.-Y. Cho, and T. W. Noh, *Orbital-dependent polaron formation in the relativistic Mott insulator Sr_2IrO_4*, Phys. Rev. B **90**, 041105 (2014).

[148] J. M. Guevara, Z. Sun, E. M. Pärschke, S. Sykora, K. Manna, J. Schoop, A. Maljuk, S. Wurmehl, J. van den Brink, B. Büchner, and C. Hess, *Spin-polaron ladder spectrum of the spin-orbit-induced Mott insulator Sr_2IrO_4 probed by scanning tunneling spectroscopy*, Phys. Rev. B **99**, 121114 (2019).

[149] P. D. C. King, T. Takayama, A. Tamai, E. Rozbicki, S. M. Walker, M. Shi, L. Patthey, R. G. Moore, D. Lu, K. M. Shen, H. Takagi, and F. Baumberger, *Spectroscopic indications of polaronic behavior of the strong spin-orbit insulator* $Sr_3Ir_2O_7$, Phys. Rev. B **87**, 241106 (2013).

[150] T. S. Nunner, B. M. Andersen, A. Melikyan, and P. J. Hirschfeld, *Dopant-Modulated Pair Interaction in Cuprate Superconductors*, Phys. Rev. Lett. **95**, 177003 (2005).

[151] M. Franz, C. Kallin, A. J. Berlinsky, and M. I. Salkola, *Critical temperature and superfluid density suppression in disordered high-*T_c *cuprate superconductors*, Phys. Rev. B **56**, 7882 (1997).

[152] P. A. Lee, *Localized states in a d-wave superconductor*, Phys. Rev. Lett. **71**, 1887 (1993).

[153] A. C. Durst and P. A. Lee, *Impurity-induced quasiparticle transport and universal-limit Wiedemann-Franz violation in d-wave superconductors*, Phys. Rev. B **62**, 1270 (2000).

[154] M. A. Sulangi, M. P. Allan, and J. Zaanen, *Revisiting quasiparticle scattering interference in high-temperature superconductors: The problem of narrow peaks*, Phys. Rev. B **96**, 134507 (2017).

[155] M. A. Sulangi and J. Zaanen, *Quasiparticle density of states, localization, and distributed disorder in the cuprate superconductors*, Phys. Rev. B **97**, 144512 (2018).

[156] Y. Wang, J. Yan, L. Shan, H.-H. Wen, Y. Tanabe, T. Adachi, and Y. Koike, *Weak-coupling d-wave BCS superconductivity and unpaired electrons in overdoped* $La_{2-x}Sr_xCuO_4$ *single crystals*, Phys. Rev. B **76**, 064512 (2007).

[157] J. W. Loram, K. A. Mirza, J. M. Wade, J. R. Cooper, and W. Y. Liang, *The electronic specific heat of cuprate superconductors*, Physica C: Superconductivity **235-240**, 134 (1994).

[158] S. Ohsugi, Y. Kitaoka, and K. Asayama, *Temperature dependence of spin susceptibility of* $La_{2-x}Sr_xCuO_4$ *Cu knight shift measurement*, Physica C: Superconductivity **282-287**, 1373 (1997).

[159] Y. Y. Peng, R. Fumagalli, Y. Ding, M. Minola, S. Caprara, D. Betto, M. Bluschke, G. M. De Luca, K. Kummer, E. Lefrançois, M. Salluzzo, H. Suzuki, M. Le Tacon, X. J. Zhou, N. B. Brookes, B. Keimer, L. Braicovich, M. Grilli, and G. Ghiringhelli, *Re-entrant charge order in overdoped* $(Bi,Pb)_{2.12}Sr_{1.88}CuO_{6+\delta}$ *outside the pseudogap regime*, Nature Materials **17**, 697 (2018).

[160] X. Li, C. Zou, Y. Ding, H. Yan, S. Ye, H. Li, Z. Hao, L. Zhao, X. Zhou, and Y. Wang, *Evolution of Charge and Pair Density Modulations in Overdoped* $Bi_2Sr_2CuO_{6+\delta}$, Phys. Rev. X **11**, 011007 (2021).

[161] A. Kopp, A. Ghosal, and S. Chakravarty, *Competing ferromagnetism in high-temperature copper oxide superconductors*, Proceedings of the National Academy of Sciences **104**, 6123 (2007).

[162] J. E. Sonier, C. V. Kaiser, V. Pacradouni, S. A. Sabok-Sayr, C. Cochrane, D. E. MacLaughlin, S. Komiya, and N. E. Hussey, *Direct search for a ferromagnetic phase in a heavily overdoped nonsuperconducting copper oxide*, Proceedings of the National Academy of Sciences **107**, 17131 (2010).

[163] Y. Komiyama, S. Onishi, M. Harada, H. Kuwahara, H. Kuroe, K. Kurashima, T. Kawamata, Y. Koike, I. Watanabe, and T. Adachi, *Magnetic Impurity Effects on Ferromagnetic Fluctuations in Heavily Overdoped (Bi,Pb)$_2$Sr$_2$Cu$_{1-y}$Fe$_y$O$_{6+\delta}$ Cuprates*, Journal of the Physical Society of Japan **90**, 084701 (2021).

[164] T. Sarkar, D. S. Wei, J. Zhang, N. R. Poniatowski, P. R. Mandal, A. Kapitulnik, and R. L. Greene, *Ferromagnetic order beyond the superconducting dome in a cuprate superconductor*, Science **368**, 532 (2020).

[165] D. C. Ghiglia and L. A. Romero, *Robust two-dimensional weighted and unweighted phase unwrapping that uses fast transforms and iterative methods*, Journal of the Optical Society of America A **11**, 107 (1994).

[166] M. A. Herráez, D. R. Burton, M. J. Lalor, and M. A. Gdeisat, *Fast two-dimensional phase-unwrapping algorithm based on sorting by reliability following a noncontinuous path*, Applied Optics **41**, 7437 (2002).

[167] M. F. Kasim, *2D Weighthed Phase Unwrapping*, 2016, matlab central file exchange.

[168] L. Moisan, *Periodic Plus Smooth Image Decomposition*, Journal of Mathematical Imaging and Vision **39**, 161 (2010).